



HAL
open science

Dryline on 19 June 2002 during IHOP. Part I: Airborne Doppler and LEANDRE II Analyses of the Thin Line Structure and Convection Initiation

Hanne V. Murphey, Roger M. Wakimoto, Cyrille Flamant, David E. Kingsmill

► **To cite this version:**

Hanne V. Murphey, Roger M. Wakimoto, Cyrille Flamant, David E. Kingsmill. Dryline on 19 June 2002 during IHOP. Part I: Airborne Doppler and LEANDRE II Analyses of the Thin Line Structure and Convection Initiation. *Monthly Weather Review*, 2006, 134, pp.406-430. 10.1175/MWR3063.1 . hal-00069037

HAL Id: hal-00069037

<https://hal.science/hal-00069037>

Submitted on 26 Jan 2021

HAL is a multi-disciplinary open access archive for the deposit and dissemination of scientific research documents, whether they are published or not. The documents may come from teaching and research institutions in France or abroad, or from public or private research centers.

L'archive ouverte pluridisciplinaire **HAL**, est destinée au dépôt et à la diffusion de documents scientifiques de niveau recherche, publiés ou non, émanant des établissements d'enseignement et de recherche français ou étrangers, des laboratoires publics ou privés.

Dryline on 19 June 2002 during IHOP. Part I: Airborne Doppler and LEANDRE II Analyses of the Thin Line Structure and Convection Initiation

HANNE V. MURPHEY AND ROGER M. WAKIMOTO*

Department of Atmospheric Sciences, University of California, Los Angeles, Los Angeles, California

CYRILLE FLAMANT

Institut Pierre-Simon Laplace/Service d'Aeronomie, Paris, France

DAVID E. KINGSMILL

Cooperative Institute for Research in Environmental Sciences, University of Colorado, Boulder, Colorado

(Manuscript received 19 July 2004, in final form 17 January 2005)

ABSTRACT

The evolution and finescale structure of a dryline that initiated a line of thunderstorms is presented. Both the along-line variability and mean vertical structure were examined using data collected by an airborne Doppler radar and a water vapor differential absorption lidar (DIAL). The initiation of convection appeared to result from the diurnally induced easterly flow in the maritime air east of the dryline that typically develops late in the day. This flow increased the low-level convergence and allowed rising parcels of air to reach the level of free convection. The along-line variability was largely attributed to numerous misocyclones distorting the thin line of radar reflectivity by advecting dry (moist) air across the dryline south (north) of the misocyclone. The misocyclones also influenced the location of the updrafts, with most of the peak values positioned north of the circulations. As a result, these updrafts were fortuitously positioned in regions of high mixing ratio where the first convective cells initiated.

1. Introduction

Predicting the initiation of deep, moist convection has remained a challenging problem, especially during the summer months over the United States. This is well illustrated by Olsen et al. (1995). They show that the summer-season threat score (the ratio of the correctly predicted rainfall area to the total threat area), which is used to verify forecasts, drops to less than half of its winter-season value. A major reason for this difference in skill is that winter-season rain events are dominated by synoptic-scale, baroclinic disturbances that are inherently more predictable. In contrast, summer- or warm-season precipitation is dominated by smaller-

scale processes that are largely confined to the planetary boundary layer. One of the most common mechanisms to initiate convective storms is by organized lines of convergence (e.g., Purdom 1976, 1982; Wilson and Schreiber 1986; Wilson and Mueller 1993; Wilson et al. 1998). Such boundaries include synoptic-scale fronts, drylines, the leading edge of cold outflows from convection, and sea-breeze fronts. The challenge for forecasters, however, is determining 1) which boundaries will initiate convection, 2) where along the boundary convection they will initiate, and 3) exactly when the convection will initiate (Weisman and Klemp 1982; Wilson and Schreiber 1986; Rotunno et al. 1988; Stensrud and Maddox 1988; Wilson et al. 1992; Weckwerth and Wakimoto 1992; Hane et al. 1993, 1997, 2002; Wilson and Mueller 1993; Fankhauser et al. 1995; Kingsmill 1995; Wilson and Megenhardt 1997; Ziegler and Rasmussen 1998; Crook and Klemp 2000).

A number of investigators have focused on the along-line variability and suggest that there are preferred locations for convection initiation along these boundaries. Regions of enhanced updrafts have been hypoth-

* Current affiliation: Earth Observing Laboratory, NCAR, Boulder, Colorado.

Corresponding author address: Hanne V. Murphey, Dept. of Atmospheric Sciences, University of California, Los Angeles, Los Angeles, CA 90095.
E-mail: hanne@atmos.ucla.edu

esized to occur at the intersection of boundaries with horizontal convective rolls (HCRs) (e.g., Wilson et al. 1992; Atkins et al. 1995, 1998). Kingsmill (1995) hypothesized that small-scale circulations or misocyclones (circulations less than 4 km in diameter; Fujita 1981), resulting from Helmholtz shearing instability, along an outflow boundary could determine where deep convection initiates. Lee and Wilhelmson (1997) have presented numerical simulations that are consistent with this hypothesis. Other mechanisms that might provide localized upward motion along the dryline include mesoscale low pressure areas (Bluestein et al. 1988), gravity waves (Koch 1982), and “bulges” in the convergence boundary (Hane et al. 1997). The dryline is a boundary between relatively cool, moist maritime air from the Gulf of Mexico and warm, dry air originating over the Mexican plateau and is known to be a location where severe local storms can initiate (e.g., Rhea 1966; Schaefer 1974, 1986).

Most of these past studies have investigated these boundaries using surface mesonet data (e.g., Koch and McCarthy 1982; Crawford and Bluestein 1997), in situ data collected on board a research aircraft (e.g., Ziegler and Hane 1993; Hane et al. 2002), or ground-based radar data over a small region (e.g., Weckwerth and Wakimoto 1992; Wilson et al. 1992; Atkins et al. 1995). Recently, the introduction of airborne Doppler radar has allowed for a different approach to sample these phenomena. High-spatial-resolution radar reflectivity and Doppler velocity data can be collected along a significant portion of the boundary while the aircraft flies parallel to it (e.g., Atkins et al. 1998). This methodology is important in light of the aforementioned efforts to resolve the along-line variability.

The case study presented here focuses on a quasi-stationary dryline that developed on 19 June 2002 near Goodland, Kansas, during the International H₂O Project (IHOP; Weckwerth et al. 2004). An airborne Doppler radar as well as a number of other mobile research platforms converged on the dryline before and during the initiation of deep convection. The aircraft flew a box pattern around the dryline with the along-boundary legs being 75–80 km long. The dryline was characterized by a number of misocyclones during all of the sampled period. The focus of the present study is the dual-Doppler wind syntheses of the evolution of the dryline up until the time that deep convection initiated. The radar analyses are augmented by a series of dropsondes released at regular intervals along a path perpendicular to the dryline by a jet flying at midlevels. The soundings resolve the detailed kinematic and thermodynamic structure of the boundary and the local environment.

Another important aspect of this study is the water vapor field retrieved by a horizontally pointing differential absorption lidar (DIAL) that was mounted on board the same aircraft equipped with the airborne Doppler radar. Accordingly, there was a *simultaneous* collection of Doppler radar and lidar data over the same region of the dryline flown by the aircraft. Resolving the moisture field, in addition to other kinematic data, within and in the vicinity of the convergence boundaries represents a unique opportunity that has never been previously attempted. There have been several studies that have highlighted the importance of accurate estimates of water vapor in predicting convection initiation. Numerical simulations by Lee et al. (1991) and Crook (1996) suggest that changes in mixing ratio as small as 1 g kg⁻¹ have significant effects on the developing convection. Weckwerth et al. (1996) and Weckwerth (2000) question the representativeness of thermodynamic profiles based on soundings launched from point locations. They suggest that variations in mixing ratio of 1.5–2.5 g kg⁻¹ are commonly observed in the boundary layer over distances of only a few kilometers. These variations appear to be a result of circulations associated with HCRs with the largest mixing ratios confined to the updraft regions of the rolls (Weckwerth et al. 1996).

This paper is the first in a series of articles (others to be published later) documenting the events on this day. A brief description of the project and the data methodology is presented in section 2. Section 3 is a discussion of the environmental conditions and the development of convection on this day. The horizontal and vertical kinematic structure of the dryline is presented in sections 4 and 5, respectively. An analysis of the misocyclones and their effect on the along-line variability of the dryline is presented in section 6. An assessment of the moisture gradient across the dryline is given in section 7, and a discussion and summary are presented in section 8.

2. IHOP and the primary data platforms

a. IHOP

The field phase of IHOP took place during late spring and early summer of 2002 over the southern Great Plains of the United States. The main objective of IHOP was to gain a better understanding of the three-dimensional water vapor distribution in the mid- and lower troposphere. IHOP had four main components, where one was focused on convection initiation and the objective here was to better understand the processes that lead to deep, warm-season convection (Weckwerth et al. 2004). It was concluded early on in

TABLE 1. ELDORA scanning mode.

Antenna rotation rate ($^{\circ} \text{ s}^{-1}$)	75
No. of samples	60
PRF (Hz)	3000
Gate length (m)	110
Sweep-angle resolution ($^{\circ}$)	1.5
Along-track resolution (m)	~ 550
Max range (km)	50
Max unambiguous velocities ($\pm \text{m s}^{-1}$)	23.6

the planning stage that in order to sample a number of boundaries, a majority of the observing platforms deployed during IHOP would have to be mobile. The primary instruments used in this study are highlighted in the following discussion. For more information about IHOP, the reader is referred to Weckwerth et al. (2004).

b. ELDORA

The National Center for Atmospheric Research (NCAR) maintains and operates a 3-cm airborne Doppler radar referred to as the Electra Doppler Radar (ELDORA). ELDORA is equipped with two antennas mounted on board a Naval Research Laboratory (NRL) P-3 aircraft. The antennas scan slightly fore and aft of the normal to the fuselage of the aircraft by $\sim 18.5^{\circ}$ so that the sweeps are nearly vertical but are actually conical. ELDORA uses a multiple-beam scanning technique known as fore-aft scanning (FAST; Jorgensen et al. 1996) in order to collect data that can be used in a dual-Doppler wind synthesis. A list of ELDORA's scanning parameters during IHOP is shown in Table 1. For more information regarding ELDORA's hardware and design, the interested reader is referred to Hildebrand et al. (1994, 1996).

ELDORA is capable of detecting echoes and Doppler velocities within the "clear air" (Wakimoto et al. 1996). This capability was critical since convergence boundaries often appear as radar-detectable thin lines (e.g., Wilson and Schreiber 1986) even in the absence of precipitation particles. The P-3 flight plan, during convection initiation missions, was to fly rectangular box-shaped flight tracks at low levels [450–600 m above ground level (AGL); hereafter, all heights are AGL] along the convergence boundaries. The long legs of the box were 75–80 km long and parallel to the thin line. The thin line was located 2–3 km from the aircraft if the pattern was executed correctly. This flight pattern was difficult to achieve owing to the nonlinear nature of many of the boundaries; hence, the mission scientist was required to make continuous corrections to the aircraft heading in flight.

The advantage of the P-3 flight track was the ability to resolve the kinematic variability of the convergence

boundaries in the along-line direction over an extended path. The main disadvantage was the time required to execute one leg (~ 12 min), which decreased the temporal resolution. Fortunately, ground-based mobile radars deployed during IHOP were positioned approximately in the center of the P-3 analysis areas. Their mission was to collect high temporal data, albeit in a much smaller domain. The findings of the ground-based facilities will be reported in a companion paper to be published later.

c. LEANDRE II

Lidar pour l'Etude des Interactions Aérosols Nuages Dynamique Rayonnement et du Cycle de l'Eau (LEANDRE II; translated as lidar for the study of aerosol–cloud–dynamics–radiation interactions and of the water cycle) is a water vapor DIAL developed at the Service d'Aéronomie (Paris) in cooperation with the technical division of the Institut National des Sciences de l'Univers (INSU) and was funded by the Centre National d'Etudes Spatiales (CNES). The lidar was mounted on the same aircraft as ELDORA during IHOP. The details concerning the design of the LEANDRE II system and the standard DIAL signal processing are given in Bruneau et al. (2001) and are only briefly presented here. The DIAL technique makes use of a laser probing the atmosphere at two wavelengths; one wavelength (so-called on-line) is centered on a water vapor absorption band and the other wavelength (so-called off-line) is positioned outside of the absorption band to act as a reference for the scattering and extinction properties of the atmosphere. The water vapor mixing ratio is determined from the difference of the slopes of the backscatter on- and off-line signals. The LEANDRE II system includes a tunable laser whose emission is positioned precisely upon an absorption line selected from two rotation-vibration bands in the near infrared (727–770 nm). As discussed in Bruneau et al. (2001), LEANDRE II characteristics (summarized in Table 2) permit water vapor mixing ratio measurements to be made with a precision better than 0.5 g kg^{-1} in the 0–5-km-distance (from the aircraft) range and an along-beam resolution of 300 m.

On 19 June, horizontal DIAL measurements in the convective boundary layer (CBL) were performed using a weak water vapor absorption band (center at 736.3 nm) to allow for the documentation of the water vapor field within a distance of 5 km from the aircraft. Because of high moisture contents in the CBL on that day, the online signal underwent significant attenuation beyond a distance of 3.5–4 km from the aircraft, which prevented any reliable water vapor mixing ratio measurements beyond that range. At close range, two fac-

TABLE 2. Main characteristics of the LEANDRE II system.

Emitter*	Spectral range	727–770 nm
	Pulse energy	$2 \times 50 \text{ mJ} \pm 10\%$
	Repetition rate	10 Hz
	Temporal pulse width	225 ns
	Double-pulse temporal separation	50 μs
	Double-pulse spectral separation	442 pm
	Spectral positioning accuracy	<0.25 pm ($5 \times 10^{-3} \text{ cm}^{-1}$)
Spectral purity	>99.99%	
Receiver	Telescope diameter	30 cm
	Field of view	1.5–8 mrad
	Photomultiplier efficiency	4%
	Filter max transmission/ bandwidth	57%/1 nm
	Digitizer	12 bits/10 MHz

* Double-pulse dual-wavelength flash-lamp-pumped alexandrite laser.

tors have an impact on the distance from the aircraft beyond which relevant water vapor mixing ratio measurements can be retrieved, namely, the saturation of the lidar signal and the geometric factor of the lidar system. The latter (former) dominates whenever the LEANDRE II is operated from the free troposphere (planetary boundary layer). The coaxial configuration of the emitter and the receiver enables the geometric factor of the lidar to approach unity at ranges as short as 600 m when LEANDRE II is operated from the free troposphere.¹ This means that there exists a “blind zone” comprised between 0 and 600 m from the aircraft in which no relevant water vapor mixing ratio measurements can be made. Whenever LEANDRE II is operated in the CBL, the number of submicronic scatterers (to which the lidar signal is proportional) being much larger than in the free troposphere (10^2 – 10^4 on average), the lidar signal is saturated on both the on- and off-line on a much longer distance than in the free troposphere, reaching 1.2 km (along the lidar line of sight) in the present case (it is on the order 0.3 km or less whenever LEANDRE II is operated from the free troposphere). The lidar could point in a vertical mode or horizontally out of the right side of the aircraft; however, the latter was chosen during the convection initiation missions.

The water vapor fields were interpolated onto a Cartesian grid using a two-pass Barnes filter (Barnes 1973)

¹ This is achieved through a so-called alignment procedure that consists of optimizing the overlap between the telescope and the laser beam field of views.

with a smoothing parameter of 600 m in the along-beam direction and 1.6 km in the along-track direction. The convergence parameter was set to 0.3. These parameters were chosen so that the resolution of the moisture plots were comparable to the ELDORA wind syntheses.

3. Environmental conditions and the development of convection

A slowly propagating cold front was forecast to move into the northwestern corner of Kansas by the early afternoon on 19 June. Surface data superimposed onto the satellite image from 1900 UTC 19 June (hereafter, all times are UTC) shows the cold front is located near Goodland, Kansas (Fig. 1a) (note the northerly post-frontal flow in eastern Colorado and southwestern Nebraska). Subsequently, the cold front stalled and became quasi-stationary during the analysis times presented in section 4. The front did not appear to have played an active role in the initiation of convection along the dryline later in the day. Low-level moisture was being advected into Kansas from Oklahoma ahead of the front by strong southerly flow. Also present on this day was a narrow, dry tongue of air separating the cold front from the moist, southerly flow. (Note the dewpoint temperature of the surface station just north of the line of clouds in Fig. 1a). A dryline was located at the eastern edge of the dry tongue. Upper-air analysis (not shown) revealed a 500-mb trough over eastern Montana and Wyoming but it appeared to be too far north to have resulted in any significant large-scale lifting over northwestern Kansas.

The positions of the dryline and cold front are shown in the surface plot superimposed onto the radar reflectivity pattern at 1900 based on the data collected by the Weather Surveillance Radar-1988 Doppler (WSR-88D) located at Goodland (Fig. 2a). The flight track of the P-3 as it approached northwest Kansas is also shown in the figure. The winds shifted from southerly to southwesterly when the aircraft penetrated the dryline. There was another dramatic wind shift to a more westerly direction farther to the west along the flight track in Fig. 2a. This wind shift was determined to be the location of the cold front. The reflectivity data in Fig. 2a shows a developing thin line at the dryline; however, no equivalent feature can be seen near the cold front. Indeed, the WSR-88D images never resolved a thin line associated with the cold front during the entire day, although its position was apparent in the surface analyses and vertical cross section based on a series of dropsondes to be shown later.

After penetrating the cold front, the P-3 reversed its

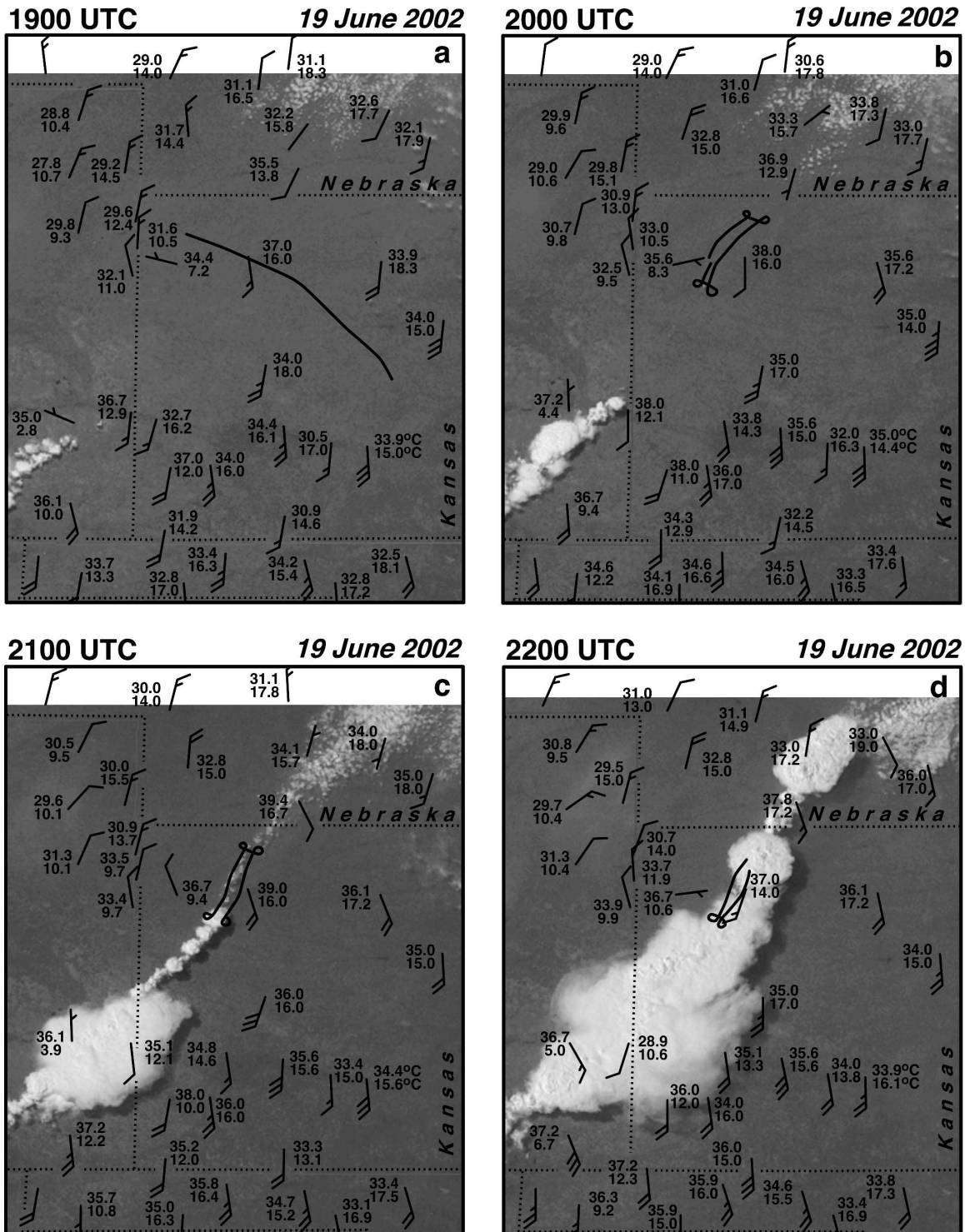


FIG. 1. Temperature and dewpoint temperature ($^{\circ}\text{C}$) superimposed on visible satellite images at (a) 1900, (b) 2000, (c) 2100, and (d) 2200 UTC 19 Jun 2002. Wind vectors are plotted with the full and half barb representing 5 and 2.5 m s^{-1} , respectively. The black line represents the flight track of the NRL P-3. The dashed lines denote the state borders.

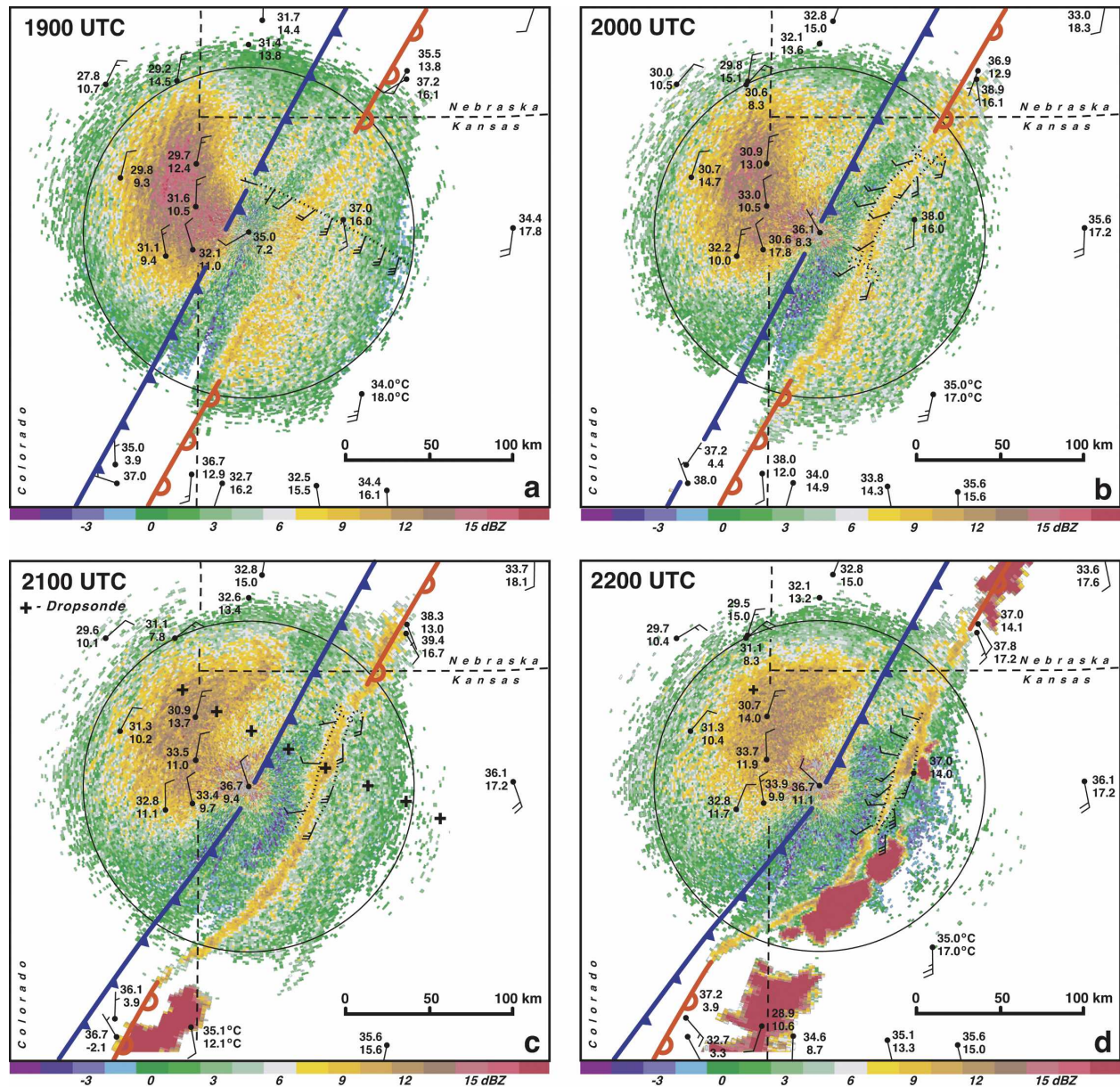


FIG. 2. Surface analyses superimposed onto surveillance scans of radar reflectivity from the WSR-88D located at Goodland, KS, at (a) 1900, (b) 2000, (c) 2100, and (d) 2200 UTC 19 Jun 2002. Temperature, dewpoint temperature ($^{\circ}\text{C}$), and wind speed and direction are plotted. Wind vector notation is the same as Fig. 1. The dotted line represents the flight track of the NRL P-3. The in situ winds collected at flight level are plotted along the track. The black crosses in (c) indicate the positions of a series of drosondes deployed by a Lear jet. The circle represents the 100-km range ring from the radar. The dashed lines denote the state borders.

heading and flew back to the east to begin its initial box pattern around the dryline at ~ 1934 . The first complete box can be seen in Figs. 1b and 2b. There were no clouds forming above the dryline at this time based on observations from the flight deck and the visible satellite image at 2000. Farther to the southwest over Colorado, however, the clouds that formed along the dryline at 1900 are in the early stages of thunderstorm

development (Fig. 1b). By 2000, the thin line produced by the dryline is better defined in the radar reflectivity field (Fig. 2b) and is associated with a wavelike pattern.

Clouds began to form along the dryline by 2100 (Fig. 1c). In addition, deep convection began to enter the southern portion of the box defined by the flight track. The first confirmed echo associated with the initiation of convection within the analysis domain observed by

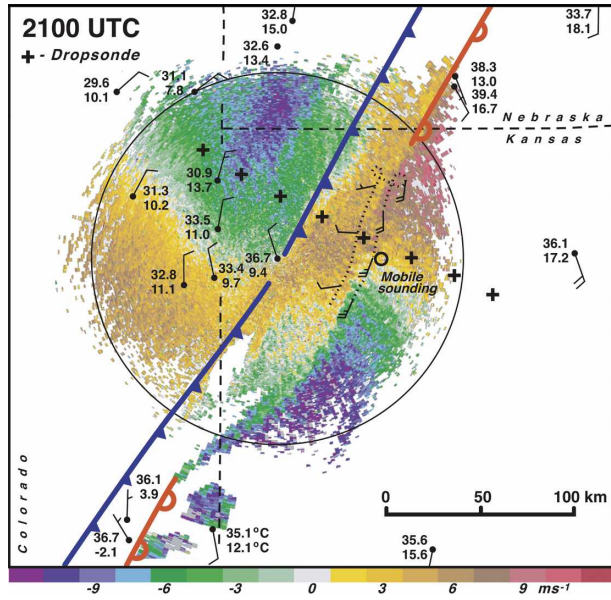


FIG. 3. Same as Fig. 2c except the analyses are superimposed on a surveillance scan of single-Doppler velocity at 2100 UTC 19 Jun 2002.

ELDORA was recorded at 2052 (Wakimoto et al. 2004, see their Fig. 5). The dryline has developed a slight eastward bulge reminiscent of those documented by Hane et al. (1997) in Fig. 2c. By 2200, deep convection had formed above and just to the east of the dryline along the P-3 flight track (Figs. 1d and 2d). The final flight leg terminated at 2205 as the mission scientist on

board the P-3 determined that the danger of flying so close to deep convection was too great.

The dryline can also be clearly identified in the low-level surveillance scan at 2100 by the discontinuity in single-Doppler velocities (Fig. 3). The northerly flow to the west of Goodland, behind the cold front, can also be seen in the Doppler velocities. Further, the wind shift associated with the cold front is seen in the top half of the figure as the flow changes from northerly behind the front to westerly in the dry slot. Closer inspection of the velocity pattern along the dryline reveals small-scale variability of the kinematic structure along the dryline. Small perturbations in velocity (i.e., the scalloped appearance near the southern portion of the flight track) along the dryline suggest the presence of circulations, which is confirmed by the results shown in section 4.

Another view of the evolution of convection on this day within the area flown by the P-3 is shown in Fig. 4. These horizontal plots are based on the ELDORA analysis at a height of 6 km, which is a better level for depicting the developing echoes. Large echoes have developed by 2122–2132 near the southern section of the domain, but only small, relatively weak echoes were observed along the majority of the track. Approximately 15 min later, however, rapid development occurred along most of the flight track between 2137 and 2149, and an almost continuous line of echoes has developed by 2154–2204.

The black crosses on Figs. 2c and 3 represent the

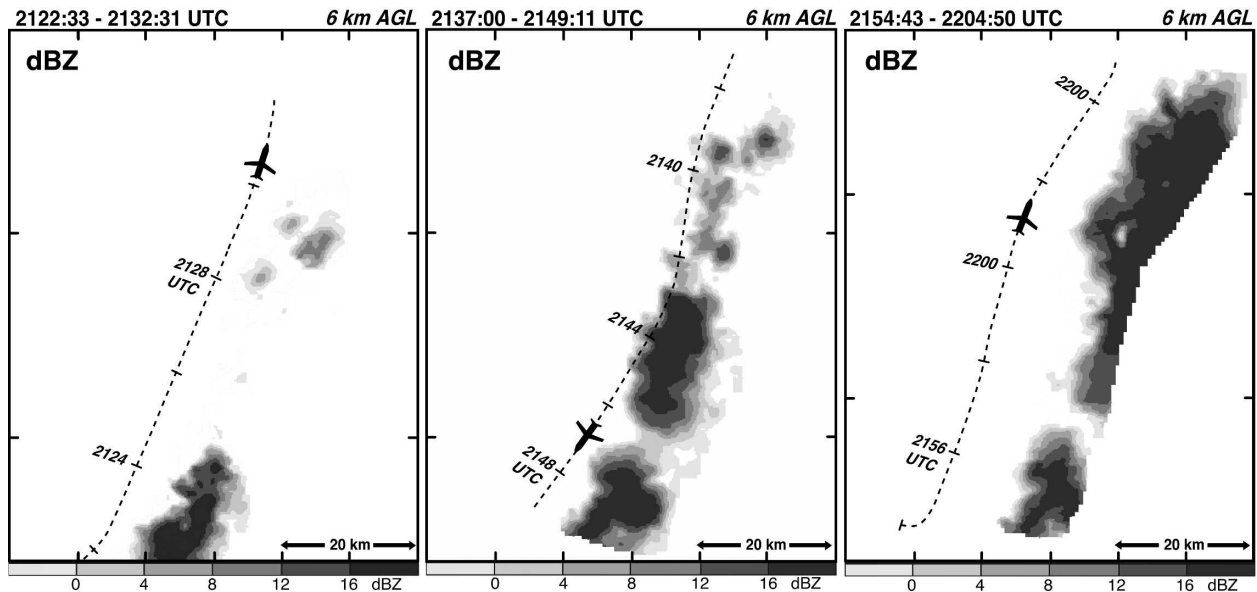


FIG. 4. Plot of the radar reflectivity recorded by ELDORA at 6 km AGL based on the last three flight legs along the dryline. The dashed line represents the flight track.

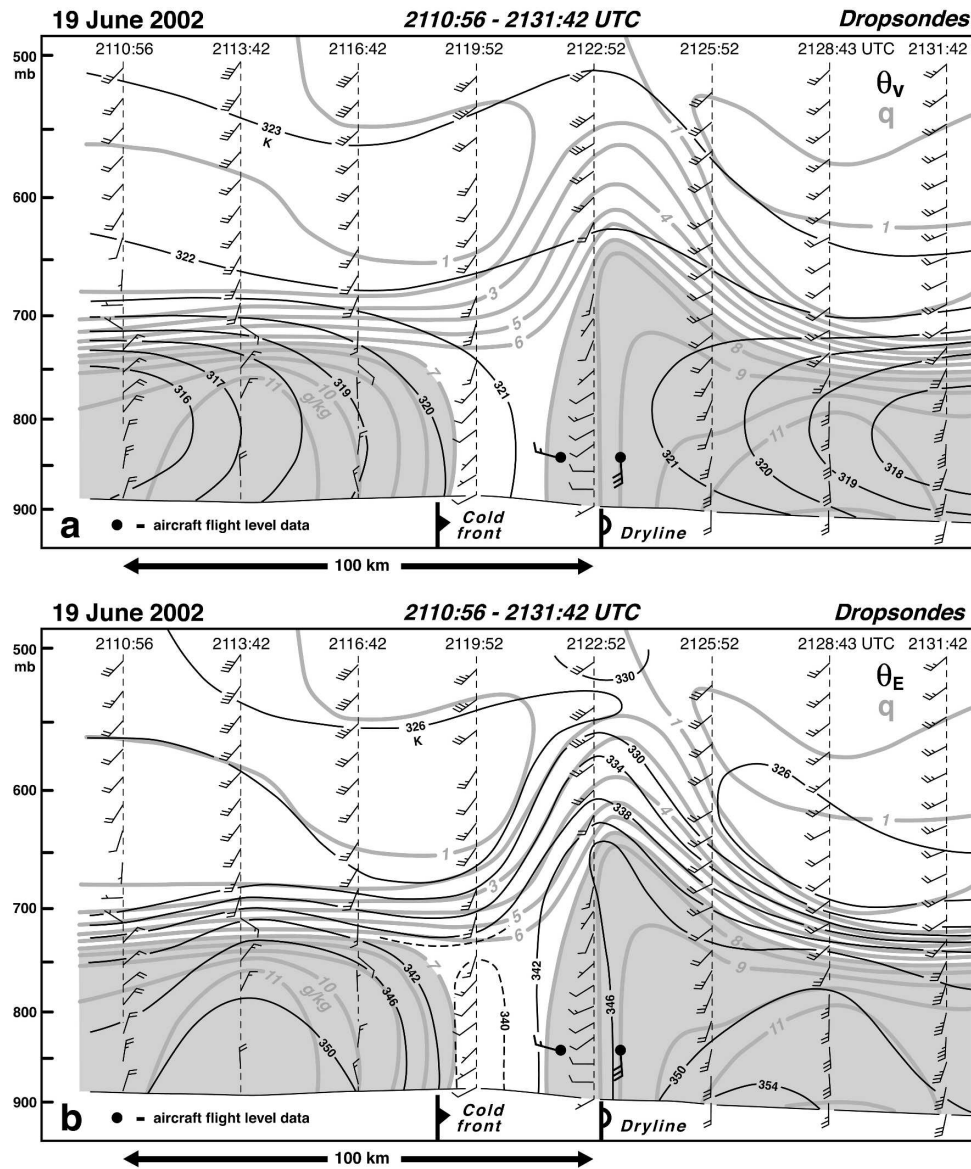


FIG. 5. Northwest-southeast cross section of winds, mixing ratio (gray lines), and (a) virtual potential temperature and (b) equivalent potential temperature across a cold front and dryline on 19 Jun 2002 based on a series of dropsondes deployed from an aircraft. Dropsonde locations are shown in Figs. 2c and 3. The release times of the dropsondes are shown at the top of the figure. Black dots represent the positions of the penetrations through the cross section by the NRL P-3. Mixing ratio values greater than 7 g kg^{-1} are shaded gray. Wind vector notation is the same as Fig. 1.

deployment locations of a series of dropsondes released by a jet flying at $\sim 500 \text{ mb}$ between 2110 and 2132. The dropsondes positions are separated by $\sim 25 \text{ km}$ and form a perpendicular line across both the cold front and the dryline. The dropsondes were deployed at the time when echoes associated with the convection were developing along the entire section of the dryline sampled by ELDORA (see Fig. 4).

Three distinct air masses can be identified in the

analysis of the winds and thermodynamic fields shown in Fig. 5a. The post-cold-frontal air was characterized by cool, moist conditions and persistent northerly flow up to a depth of 750 mb. Relatively cool and moist conditions associated with southerly flow were also noted east of the dryline. Both of the cool air masses are capped by strong stable layers as indicated by the packing of the isopleths of virtual potential temperature (θ_v). The air mass between the two boundaries

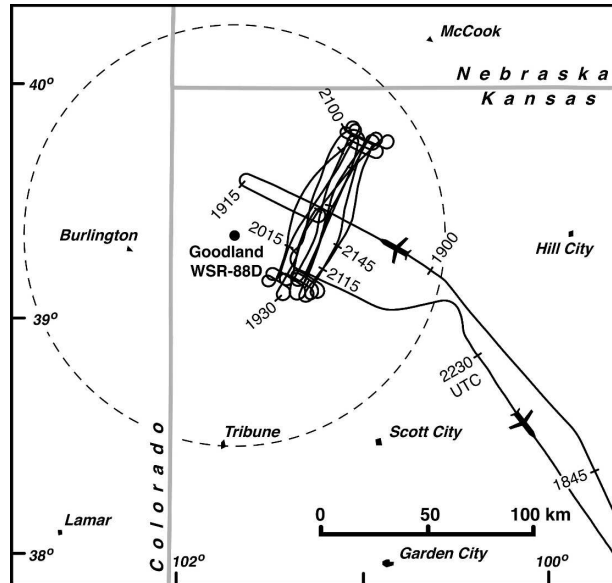


FIG. 6. The flight track of the NRL P-3 on 19 Jun 2002. The gray lines denote the state borders. The black dot represents the location of the Goodland, KS, WSR-88D, and the dashed circle represents the 100-km range ring from the radar.

(i.e., the dry tongue) is warm, relatively dry, and accompanied by west-southwesterly winds. The location where convection initiates is denoted by the upward bulge in the isopleths of mixing ratio (q) and θ_v . This is also the region where the boundary layer is well mixed up to the ~ 650 mb level and capped by a weak stable layer. Similar moisture bulges have been observed (Schaefer 1974, 1986; Ziegler and Hane 1993; Ziegler and Rasmussen 1998) and simulated (Ziegler et al. 1997) and were attributed to deep convergence and updrafts. The entire region shown in Fig. 5b is potentially unstable as shown by the analysis of equivalent potential temperature (θ_E). The isopleths of θ_E mimic the upward bulge in q in the region where convection is initiating. The lowest values of θ_E are found in the dry tongue between the cold front and dryline.

4. Horizontal analyses of the kinematic evolution of the dryline

The entire flight track of the P-3 on 19 June is shown in Fig. 6. The flight path of the aircraft and ELDORA's

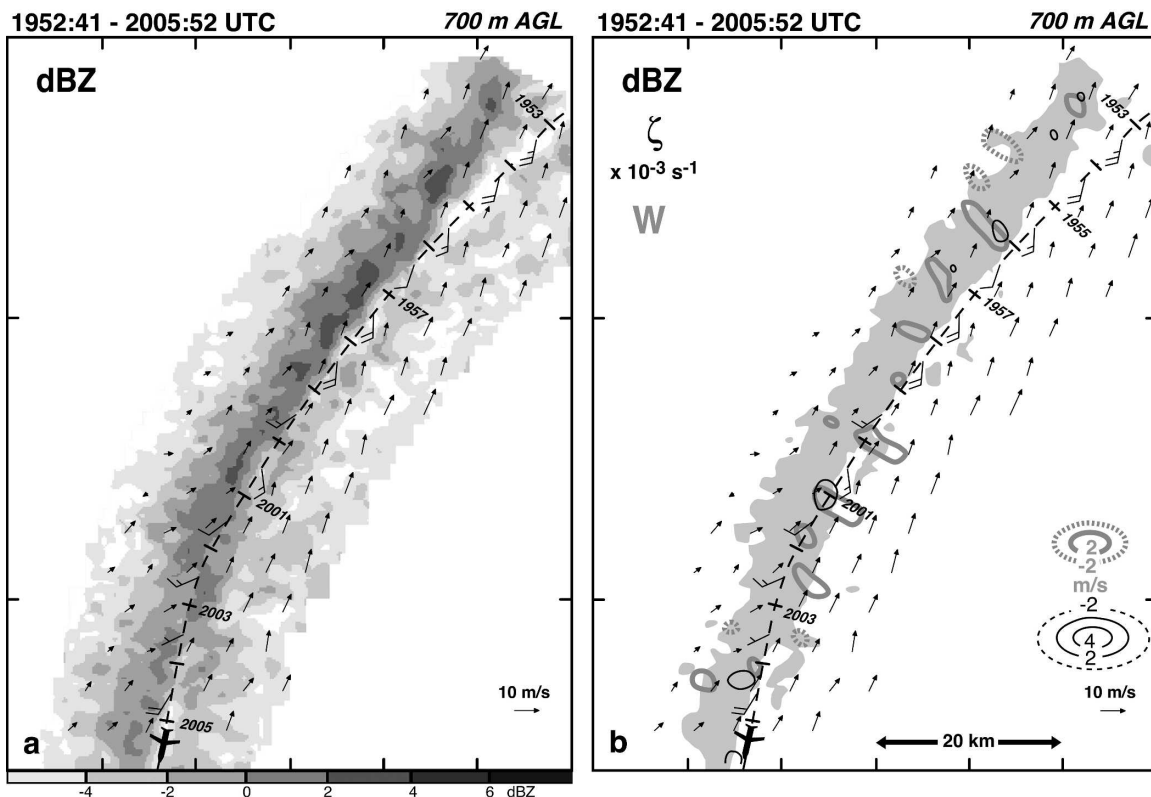


FIG. 7. Dual-Doppler wind synthesis at 1952:41–2005:52 UTC at 700 m AGL. (a) Radar reflectivity. (b) Vertical velocity and vorticity. The dashed black line represents the track of the P-3. Flight-level winds are plotted along the track. Wind vectors are plotted with the full barb and half barb representing 5 and 2.5 m s^{-1} , respectively. Positive and negative vertical velocities are drawn as gray and dashed gray lines, respectively. Positive and negative vertical vorticity are drawn as black and dashed-black lines, respectively. Radar reflectivities greater than -2 dBZ are shaded gray in (b).

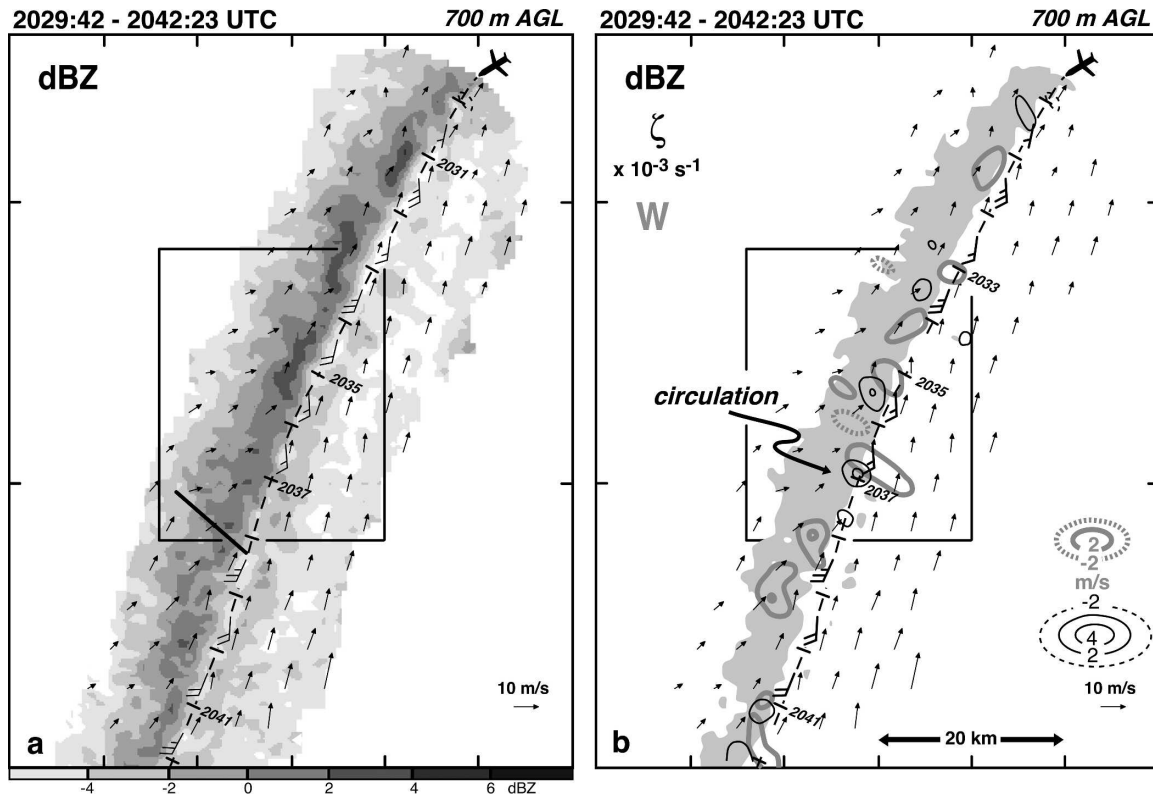


FIG. 8. Same as Fig. 7 except for 2029:42–2042:23 UTC at 700 m AGL. The black line in (a) represents the location of the cross section shown in Fig. 9. Black box is enlarged in Fig. 18.

ability to detect clear-air echoes resulted in excellent dual-Doppler wind syntheses for each of the nine along-boundary legs for a period covering ~ 3 h. In addition, dual-Doppler syntheses were created for some of the shorter, across-boundary legs shown in the figure. The details of the radar methodology are presented in the appendix.

a. 1952–2006 UTC

The first leg flown along the dryline was between 1934 and 1946 when the aircraft was flying north paralleling the western side of the dryline. The wind synthesis for the next leg (1952–2005) at 700 m is presented in Fig. 7. The P-3 was heading south within the moist air east of the dryline at this time. The radar was typically able to detect clear air returns out to a range of ~ 15 km on this day. The thin line and wind shift associated with the dryline is apparent in Fig. 7a. There are embedded pockets of higher reflectivity within the thin line that are near updraft regions (Fig. 7b) as shown by Christian and Wakimoto (1989) and Wilson et al. (1994).

Also apparent in Fig. 7b are small maxima in vertical vorticity or misocyclones. Misocyclones along convergence boundaries have been noted by a number of in-

vestigators (e.g., Carbone 1982; Mueller and Carbone 1987; Wakimoto and Wilson 1989; Kingsmill 1995) and have been numerically simulated by Lee and Wilhelmson (1997). In this case, it is believed that the circulations were a result of Helmholtz shearing instability and were moving northeastward along the boundary at ~ 6 m s $^{-1}$. Linear theory suggests that the fastest-growing mode for this type of instability will be at a wavelength ~ 7.5 times the transition zone width (Miles and Howard 1964). The wind speed and direction data for all in situ penetrations of the dryline by the P-3 were examined (not shown). The width of the shear zone based on the flight-level data varied between 990 and 2410 m, suggesting wavelengths between 7.4 and 18.1 km for the fastest-growing mode. The observed spacing of the misocyclones varied between 3.8 and 14 km, which is close to the values predicted by linear theory.

Misocyclones can also form when HCRs are tilted into the vertical by updrafts along a convergence boundary. To examine this mechanism, radar reflectivity data from the Goodland WSR-88D was objectively analyzed to determine the orientation of the HCRs east of the dryline using a technique proposed by Fankhauser et al. (1995). The data were cross corre-

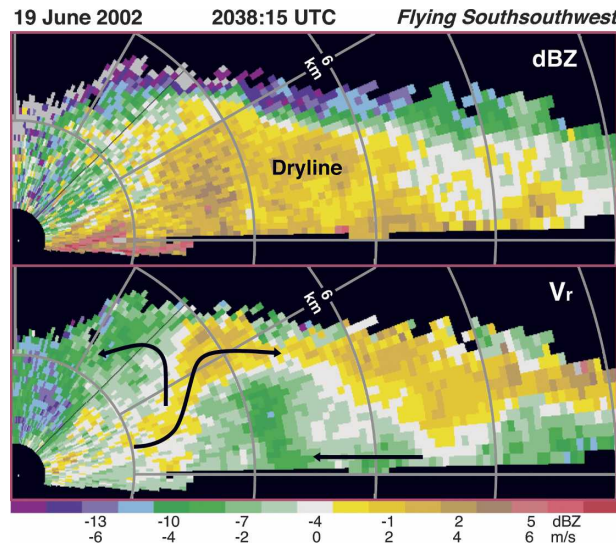


FIG. 9. RHI cross section of (top) radar reflectivity and (bottom) single-Doppler velocity through the dryline at 2038:15 UTC. Approximate flow pattern shown by the black arrows is based on single-Doppler velocities. The location of the scan is shown in Fig. 8a. Gray lines are the range rings and angles from the aircraft.

lated with a cosine function using a wavelength of 8 km. The analysis (not shown) revealed that the HCRs were approximately parallel to the boundary and did not appear to intersect the dryline.

The misocyclones are generally not collocated with updraft regions, consistent with the past studies mentioned earlier (an exception is the misocyclone near 2001 along the flight track). There are two explanations for the observed displacement between misocyclones and the updraft maxima. The maximum vorticity within the misocyclones is greatest at low levels (not shown). Klemm and Rotunno (1983) have argued, using the diagnostic perturbation pressure equation, that strong circulations near the surface lower the dynamic perturbation pressure and can produce a downward-directed pressure gradient. A downdraft may develop if the latter is the dominant term in the vertical momentum equation (e.g., Mueller and Carbone 1987; Lee and Wilhelmson 1997); however, weaker pressure gradients may reduce the updraft speeds.

A second explanation for the observed displacements has been proposed by Lee and Wilhelmson (1997). If the flow across the convergence boundary is asymmetric, misocyclones circulations will distort a boundary

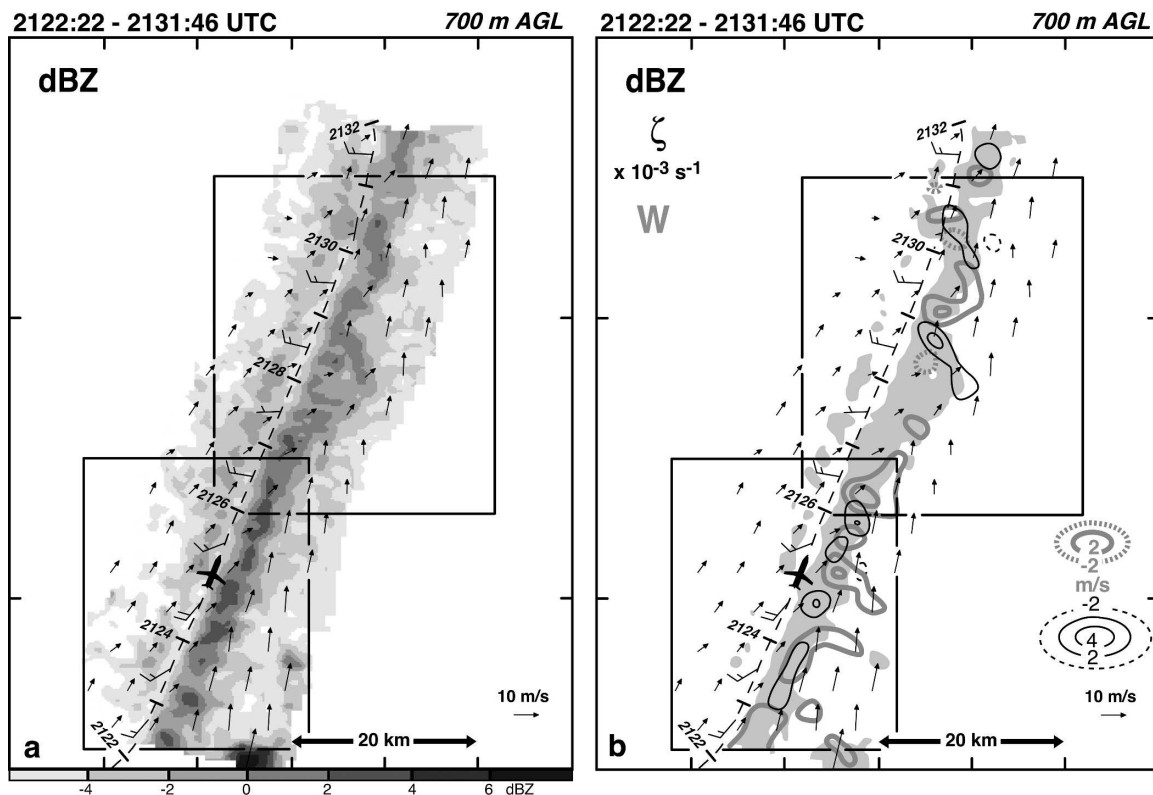


FIG. 10. Same as Fig. 7 except for 2122:22–2131:46 UTC at 700 m AGL. Top and bottom black boxes are enlarged in Figs. 19 and 18, respectively.

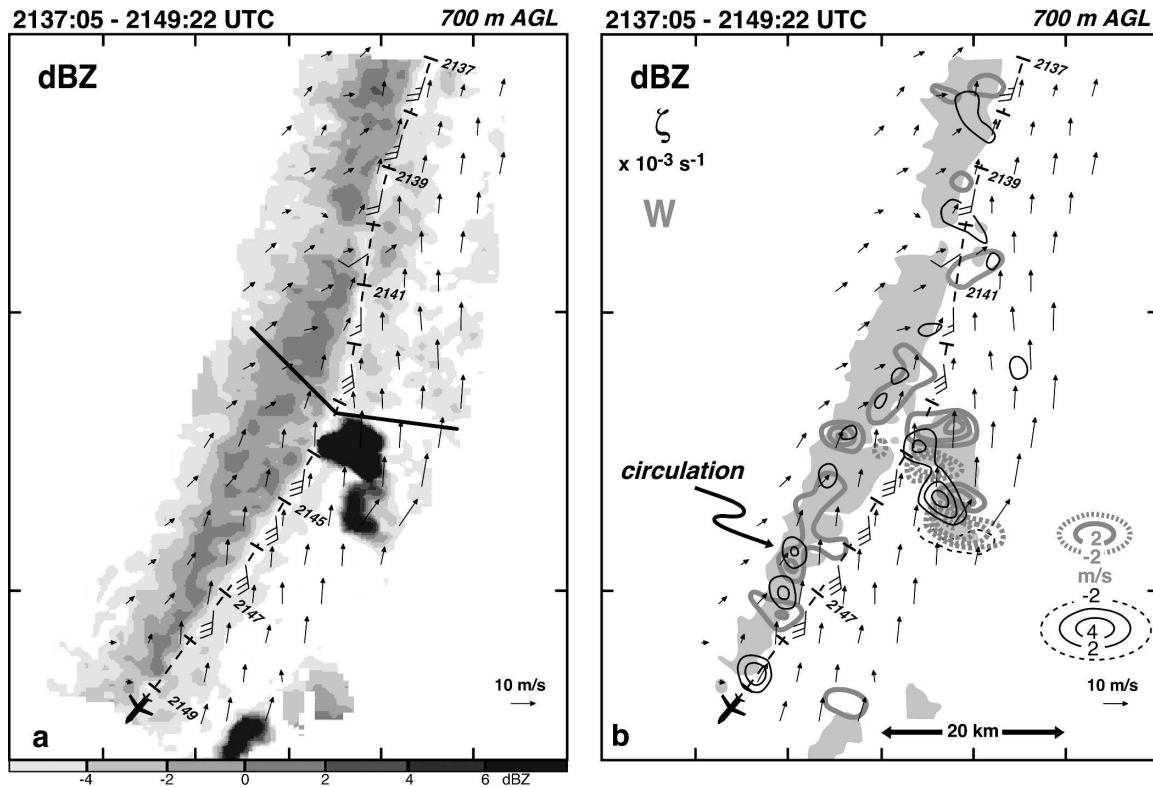


FIG. 11. Same as Fig. 7 except for 2137:05–2149:22 UTC at 700 m AGL. Black lines in (a) indicate the position of the aft scan shown in Fig. 12. Black arrow indicates the position of a circulation. Vertical cross sections through this circulation are shown in Fig. 17.

and result in preferred regions of enhanced convergence and updrafts. A similar mechanism was suggested by Hobbs and Persson (1982) and Wakimoto and Bosart (2000) for explaining the updraft structure along cold fronts that exhibit a precipitation core/gap structure.

The difficulty of navigating the P-3 close to and parallel to the thin line is illustrated in Fig. 7. The pilots were instructed by the mission scientist to make several corrections to the heading starting at ~ 2001 in order for the aircraft to remain on the moist side of the boundary. The aircraft would occasionally drift to the dry side of the boundary, which is clearly seen by the shift in the wind direction to a more westerly component in the flight-level data (Fig. 7). The shifts in wind were also accompanied by significant drops in mixing ratio (not shown).

It should be noted that the winds west of the dryline are not from a uniform direction. An example of this can be seen in the dual-Doppler winds between 2002 and 2004 along the flight track. The wind synthesis shows a more westerly component in this segment (Fig. 7a). As a result, the dryline advanced farther to the east in this region, contributing to the inadvertent aircraft crossing to the dry side of the boundary.

b. 2029–2042 and 2122–2132 UTC

The synthesis for the fourth flight leg is presented in Fig. 8. The thin line was quasi-stationary but is more linear than the previous pass. Several of the misocyclones and the updrafts have strengthened to values $>4 \times 10^{-3} \text{ s}^{-1}$ and 4 m s^{-1} , respectively (Fig. 8b). The stronger misocyclones tend to be located south of the updraft maxima and the nonuniformity of the winds on the western side of the dryline is more pronounced.

The vertical structure of the dryline is revealed in one of the raw scans collected by ELDORA (Fig. 9). The thin line associated with the dryline is $\sim 2.5 \text{ km}$ deep and $4\text{--}5 \text{ km}$ wide with maximum radar reflectivities of $\sim 5 \text{ dBZ}$. The single-Doppler velocities suggest low-level convergence and upper-level divergence at the boundary as shown by the black arrows.

The analysis of the seventh leg (2122–2131) provides one of the better examples of the along-line variability of the dryline. The echoes are stronger along the southern half of the thin line (Fig. 10a), suggesting stronger convergence and enhanced updrafts (Wilson et al. 1994) as shown in Fig. 10b. A significant storm was developing east of the dryline along the southern edge

of the domain (Fig. 10a) and radar echoes accompanying the intensifying storms were developing at higher levels above the aircraft (Fig. 4).

Of particular interest is a small eastward bulge in the thin line, approximately 10 km long, centered at 2128 along the flight track. The dual-Doppler winds within the bulge indicate a stronger westerly wind component perpendicular to the convergence boundary. Moreover, a peak in vertical vorticity associated with a misocyclone is located on the northern fringe of the bulge. Additional analyses on this reflectivity bulge will be presented in section 6.

c. 2137–2149 UTC

Numerous storms were detected aloft during the next pass along the dryline from 2137 to 2149 (Fig. 4). Several of these storms were beginning to produce light precipitation at low levels (Fig. 11a). An example of the vertical structure of one of these storms is presented in Fig. 12. The structure resembles a mantle echo (Atlas 1959; Knight and Miller 1993) with peak radar reflectivities reaching only 27 dBZ even though the echo tops extends to 14 km. The term “mantle” describes the configuration of the echo, which often appears as an inverted-U shape in a vertical cross section and corresponds to the outer boundaries of the cumulus clouds.

The maximum speeds within the narrow updraft, collocated with the weak-echo vault, are estimated from the single-Doppler velocities to be 44 m s^{-1} . No correction for terminal fall speed was applied to the vertical velocities since the radar reflectivities are weak. There are streamers of echo that emanate from the reflectivity thin line and are entrained into the updraft. Wakimoto et al. (2004) hypothesized that these streamers were insects—a major contributor to echo return within thin lines (e.g., Wilson and Schreiber 1986; Wilson et al. 1994)—that are being swept up into the intense updrafts. In contrast, the two filaments of echo at low levels (located at a range between 3 and 6 km) on the other side of the aircraft denote areas where light precipitation is falling to the ground. This conclusion is supported by the presence of a bright band. The single-Doppler velocities also show an area of negative Doppler velocities below the bright band owing to the increased terminal fall speeds of the raindrops.

The echo bulge noted in the previous pass has evolved into a complete “break” in the thin line at $\sim 2140:30$ along the flight track in Fig. 11. The dual-Doppler winds show stronger westerly flow through the gap in the thin line, which was also indicated by the flight-level winds. The misocyclones are numerous and prominent along the entire length of the thin line. Sev-

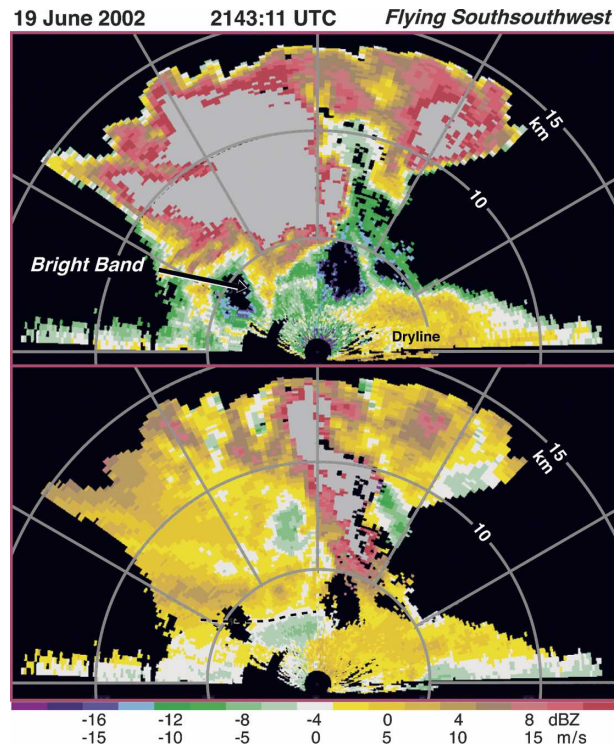


FIG. 12. ELDORA tail radar scan at 2143:11 UTC through the dryline and developing convection. (top) Radar reflectivity and (bottom) single-Doppler velocity are displayed. Gray lines are the range rings and angles from the aircraft. The location of the scan is shown in Fig. 11a. The position of a bright band is shown by the arrow and dashed line on the top and bottom panels, respectively. Gray shading represents values that are off the color scale.

eral misocyclones appear to be collocated with updrafts along the southern portion of the thin line. A superposition of misocyclones and updrafts has been hypothesized to be the generating mechanism for nonsupercell tornadoes (e.g., Brady and Szoke 1989; Wakimoto and Wilson 1989; Lee and Wilhelmson 1997). Indeed, numerous dust devils and tornado-like circulations were observed by the scientists on board the P-3 and the ground-based mobile facilities during this and subsequent times.

d. 2154–2204 UTC

The final leg was executed by the P-3 between 2154 and 2204 (Fig. 13). Subsequent flight legs along the dryline were ruled out owing to safety concerns for the aircraft in the vicinity of deep convection that was beginning to produce intense rainshafts and outflows. The storms along the northern section of the dryline are accompanied by intense echoes aloft (Fig. 4) and at low levels. Noteworthy in the dual-Doppler synthesis is the

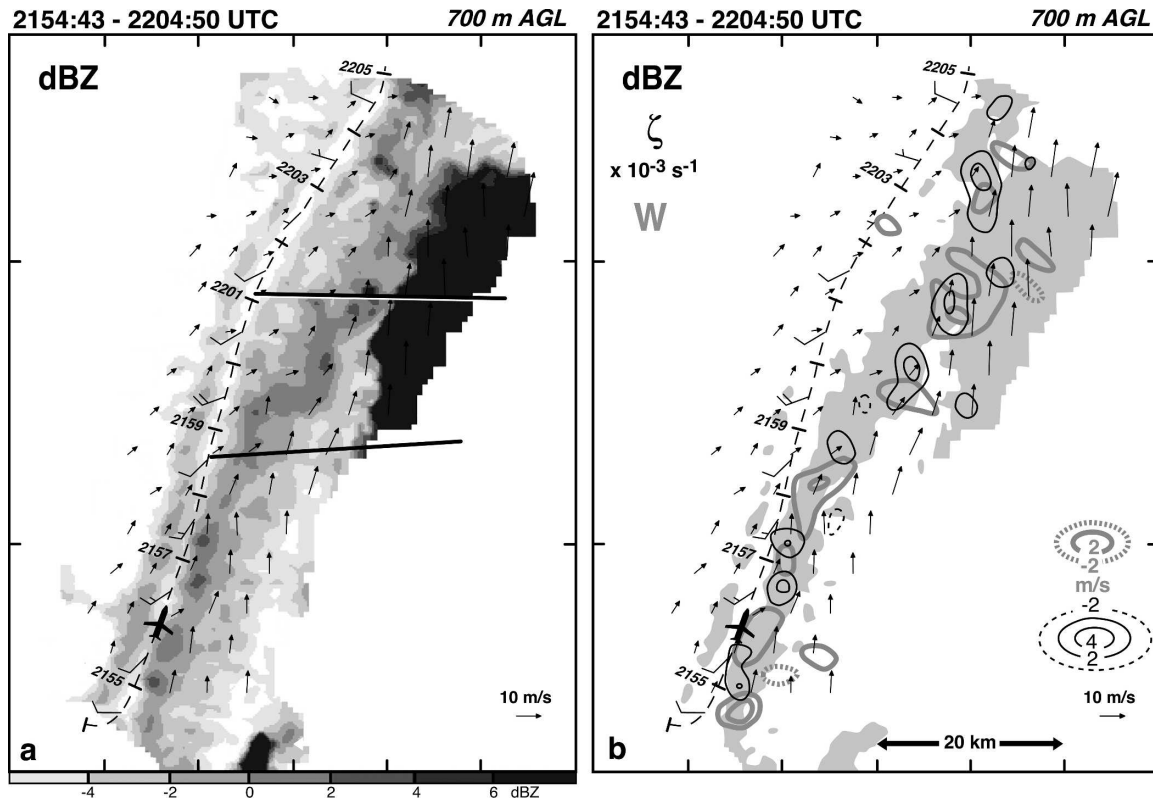


FIG. 13. Same as Fig. 7 except for 2154:43–2204:50 UTC at 700 m AGL. Black lines indicate the positions of two cross sections shown in Fig. 14.

eastward displacement of a segment of the thin line associated with the dryline (~30 km in length) from 2200 to 2204 along the flight track. An examination of vertical cross sections of dual-Doppler wind synthesis (not shown) and the individual range–height indicator (RHI) scans by ELDORA reveal that this eastward displacement was in response to the strong inflow into the developing thunderstorms. Two of the RHI cross sections are shown in Fig. 14. The cross section at 2158:33 was recorded in a region south of the eastward displacement. The second cross section at 2201:05 reveals that the location of the main reflectivity of the displaced thin line (indicated by the white arrow) is beneath the weak-echo vault and, hence, within the inflow region of the storm. The entire weak-echo vault is filled with weak radar reflectivities at the latter time as the thin line is “ingested” into the storm.

5. Vertical cross sections of the mean structure

The long legs flown by the P-3 provided an important opportunity to assess the along-line variability of the dryline. Another advantage was the ability to recon-

struct the mean vertical structure of the dryline by averaging individual vertical cross sections from dual-Doppler wind syntheses along the entire length of the flight track. The horizontal grid spacing of the Doppler analysis was 600 m (see appendix). Accordingly, mean cross sections were produced by averaging ~105 individual cross sections for each flight leg. The averaging was effective in removing the along-line variability.

The mean vertical structure of the dryline for the second pass (1952–2005) is presented in Fig. 15a. There are weak updrafts that are displaced to the eastern side of the radar-detected thin line in response to low-level convergence (less than 1 km) of the component of the wind in the plane of the cross section. This weak convergence changes into divergence at higher levels. The results presented in section 4 revealed that the convergence boundary was accompanied by numerous misocyclones along its entire length. Not surprisingly, there is a maximum in cyclonic vorticity ($>1.5 \times 10^{-3} \text{ s}^{-1}$) centered on the thin line in Fig. 15a.

The mean positive vertical vorticity has decreased slightly along the dryline but increased in width by 2104–2116 (Fig. 15b). The mean updrafts along the dryline have intensified and deepened. Recall that the

2158:33 UTC

2201:05 UTC

19 June 2002

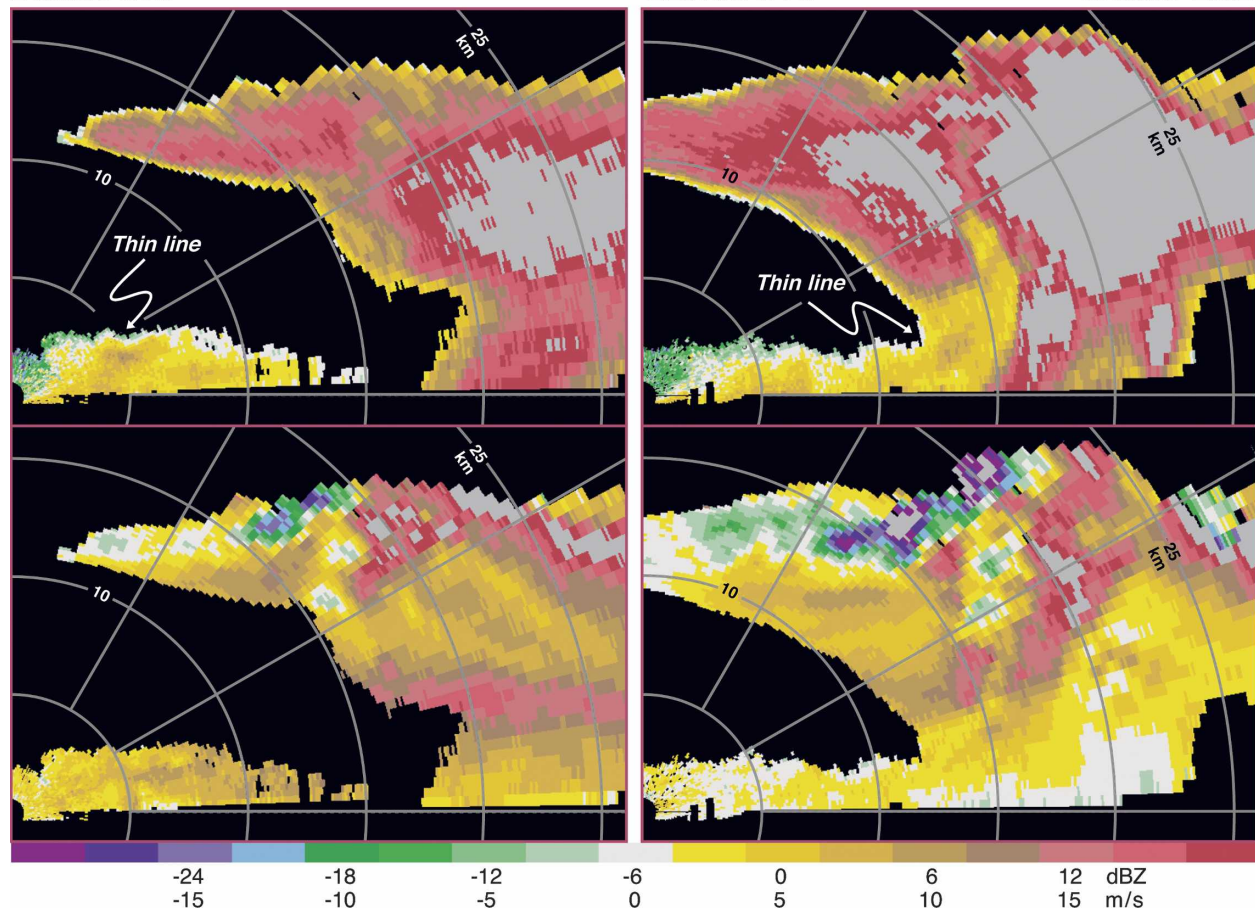


FIG. 14. Two vertical cross sections through the dryline and developing storm at 2158:33 and 2201:05 UTC. White arrow indicates the position of the radar-detected thin line. (top) Radar reflectivity and (bottom) single-Doppler velocity. Gray lines are the range rings and angles from the aircraft. Locations of the cross sections are shown in Fig. 13a. Gray shading represents values that are off the color scale.

first echoes associated with developing storms were detected by ELDORA a few minutes before this analysis time (~ 2052). The increase in updraft speed is largely attributed to the increase in the easterly component of the flow (in the rotated coordinate system) in the moist air that enhanced the low-level convergence at the dryline (Fig. 15b). Also, the divergence field (not shown) indicates a slight increase in the depth of the low-level convergence at this time. The increase in the depth of updrafts to ~ 3 km is important since the level of free convection (LFC), based on nearby soundings, was 3–3.5 km (Wakimoto et al. 2004, see their Fig. 14). This is consistent with the rapid development of strong echoes at this time.

The appearance of an easterly component of flow in the moist air during the late afternoon has been well documented (e.g., Ziegler and Hane 1993; Ziegler et al. 1995; Atkins et al. 1998; Jones and Bannon 2002). The

primary causes appear to be 1) the gradient of heating, which promotes a deeper CBL to the west of the dryline, which creates an east–west hydrostatic pressure gradient force (e.g., Ziegler and Hane 1993; Jones and Bannon 2002), and 2) the intensifying gradient of virtual potential temperature (cooler air to the east; see Fig. 5) producing solenoidal forcing in a vertical plane normal to the dryline (Ziegler and Hane 1993; Ziegler et al. 1997). Easterly flow in the moist air can exist even if the dryline is stationary or moving eastward (Miller et al. 2001; Jones and Bannon 2002). Accordingly, *the initiation of convection along the dryline appears to be a result of the diurnally induced easterly flow in the maritime air that typically develops late in the day, which increases low-level convergence and allows rising parcels of air to reach the LFC.*

The easterly flow in the moist air is stronger at 2137–2149 (Fig. 15c); however, it is being augmented by weak

outflow from the thunderstorms forming east of the dryline. The influence of the developing storms can also be seen by the secondary peak in positive vertical velocities located ~ 7 km to the east of the dryline. This peak is an extension of the thunderstorm updrafts. Indeed, the storm inflow combined with the low-level outflow has tilted the vertical axis of the cyclonic vorticity toward the storms.

6. Misocyclones and along-line variability of moisture

The existence of misocyclones combined with the closeness of the flight track to the dryline resulted in several in situ penetrations of these circulations. One of these penetrations occurred during the pass from 2029 to 2042 (see Fig. 8) and the flight-level data are plotted in Fig. 16. The approximate location of the misocyclone center is indicated on the figure as well as the horizontal extent of the $2 \times 10^{-3} \text{ s}^{-1}$ vorticity isopleth. There is descending flow near the misocyclone center, in response to the downward-directed perturbation pressure gradient discussed in section 4a.² There are updrafts surrounding the downdraft core similar to numerical simulations by Lee and Wilhelmson (1997). The wind direction shifts but does not suggest that a closed circulation was penetrated. No major discontinuities in wind speed or θ_V were noted. The variations of mixing ratio suggest that regions north and south of the misocyclone are associated with higher and lower values of moisture, respectively.

Although not the same misocyclone shown in Fig. 16, the vertical structure of another circulation was revealed by the raw ELDORA data during the pass from 2137 to 2149. The cross sections in Fig. 17 show two consecutive scans by the fore antenna separated by only 5 s. There is little change in the vertical structure of the radar reflectivity of the thin line in these two scans. In contrast, there is a striking difference in the single-Doppler velocity profiles. Each scan slices through the positive and negative velocities associated with the rotational couplet, respectively. The rotational couplet appears to be ~ 1.5 km wide and ~ 3 km deep.

A closer examination of the horizontal structure of the misocyclones combined with data from LEANDRE II is shown in Fig. 18. The discussion presented in section 2 revealed that the moisture data collected by the lidar was restricted to a very narrow swath, only a few kilometers in width. This restriction limited the amount

of usable data since the aircraft would have to be perfectly positioned and not drift away from the thin line in order to assess the variations of moisture along the boundary.

The first plot is based on the pass from 2029 to 2042 (see Fig. 8) when the P-3 was flying on the moist side of the dryline. This also represents the pass when the aircraft penetrated the misocyclone located at ~ 2037 along the flight track (see Fig. 16). Several misocyclones can be identified in Fig. 18a, and their effect on the structure of the dryline is apparent. In general, they represent an inflection point in the wind field with more westerly and easterly flow (relative to the orientation of the dryline) located south and north of the misocyclone, respectively. This is consistent with in situ measurements shown earlier in Fig. 16. Consequently, the drier (moist) air is being advected toward the east (west) side of the dryline south (north) of the misocyclone at this time. This latter statement is confirmed by the mixing ratios retrieved from LEANDRE II. Mixing ratio values greater than 10 g kg^{-1} are located north of the misocyclones near 2033:30 and 2035:30 along the flight track. The mixing ratios drop to $\sim 8 \text{ g kg}^{-1}$ south of these misocyclones. Unfortunately, no LEANDRE II information was collected for the misocyclone near 2037, since the plane penetrated the circulation and hence was too close for LEANDRE II to observe. However, the flight-level data are consistent with the previous discussion (see Fig. 16). A gradient of $\sim 1.5 \text{ g kg}^{-1}$ was recorded by the P-3 with the higher values located north of the misocyclone center.

The updrafts along the dryline are typically displaced to the north of the misocyclones in Fig. 18a as noted earlier. This displacement is fortuitous for convection initiation since the updrafts are positioned near the regions of highest mixing ratio (Fig. 18a); that is, *low-level convergence along the dryline and wind perturbations resulting from the presence of the misocyclones were determining where moist parcels of air within pockets of updrafts were being forced up to their LFC*. Recall that the first echoes associated with the developing storms were recorded by ELDORA at ~ 2052 .

Figure 18b presents an analysis of the dryline approximately one hour later. Several misocyclones are evident at this time and their centers are separated by 4–8 km. The updrafts are stronger at this time but are still generally displaced from the misocyclones. The major difference from the earlier time is the relationship between misocyclones and moisture field. There is a tendency for the moist air to be collocated with the misocyclones (Fig. 18b) with relatively drier air near the updraft centers. It is hypothesized that the echoes that are rapidly developing aloft along most of the de-

² Downdrafts within the misocyclones were not resolved in the dual-Doppler wind synthesis owing to the imposed filtering scheme discussed in the appendix. The downdraft noted in Fig. 16 is ~ 1 km in diameter.

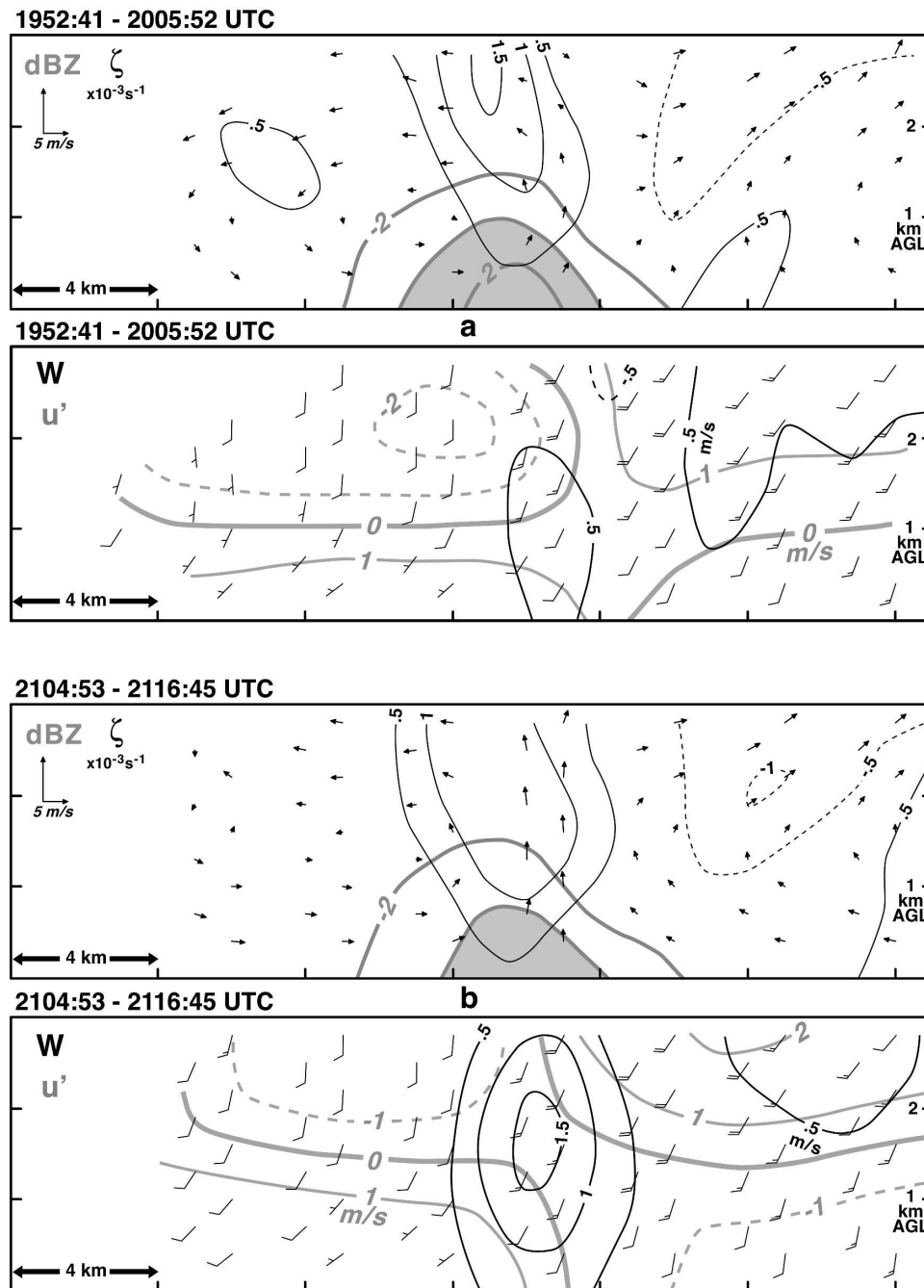


FIG. 15. Mean vertical cross sections through the dryline at (a) 1952:41–2005:52, (b) 2104:53–2116:45, and (c) 2137:05–2149:22 UTC: (top) vertical vorticity (solid and dashed black lines) and radar reflectivity (gray lines) superimposed on top of the winds in the plane of the cross section, and (bottom) vertical velocity (solid and dashed black lines) and the u component of the flow in the rotated domain (gray and dashed gray lines) superimposed on top of the total horizontal wind vectors. Radar reflectivities greater than 0 dBZ are shaded gray.

picted track (see Fig. 4) are influencing the low-level moisture distribution. The rising parcels of air feeding the intensifying storms could have depleted the moisture in the boundary layer. Accordingly, the collocation

of drier air and updrafts in Fig. 18b may not be surprising. The crosses labeled in Fig. 18b denote the location of the peak updrafts into the developing storms at a height between 5 and 8 km. The 2 m s^{-1} isopleth is also

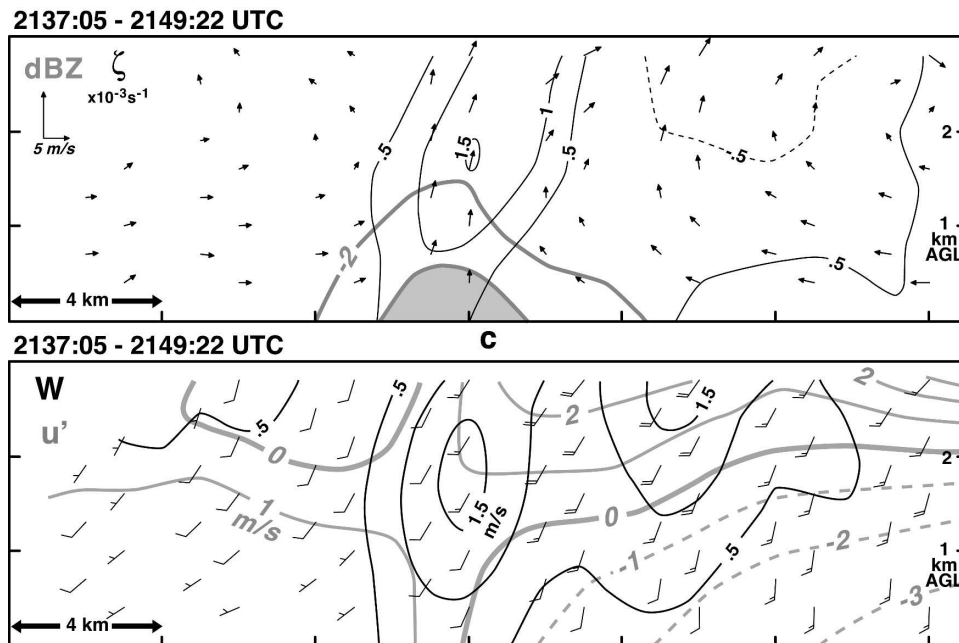


FIG. 15. (Continued)

elongated beneath these intensifying echoes. The moisture content within the misocyclones is still relatively high since the presence of a downward-directed perturbation pressure gradient would initially keep this air from rising in the developing nascent updrafts. As the storms grow, they (along with their pendant updrafts) will begin to move at a speed determined by the upper-level winds. This speed will be different than the movement of the misocyclones and will increase the likelihood that updrafts and misocyclones will be collocated and produce nonsupercell tornadoes.

The distribution of moisture along the dryline in the vicinity of the bulge discussed in section 4b is presented in Fig. 19. The first time shown is before the bulge in the thin line was apparent (Fig. 19a). Three misocyclones that are regularly spaced can be identified in the figure. The displacement between updrafts and misocyclones and the general tendency for the moist and dry air to be positioned north and south of misocyclones, respectively, is evident. Note how the misocyclones distort the thin line into a wavelike pattern (Fig. 19a). The next pass by the P-3 shows that the westerly flow south of the middle misocyclone has created the bulge in the thin line. The westerly push of dry air can be seen in the dual-Doppler wind synthesis and the lower values of mixing ratio.

7. Moisture variation across the dryline

The limited field of view of LEANDRE II hampered the assessment of the gradient of moisture across the

dryline while the P-3 was flying parallel to the thin line. This limitation was overcome by analyzing several of the short flight legs that penetrated the dryline. One of the first penetrations was between 1931 and 1933 (Fig. 20a). The slow shift in wind direction across the dryline in the flight-level data suggests that the dryline was not a sharp discontinuity during this pass (see Fig. 2a). A mixing ratio discontinuity of $\sim 2 \text{ g kg}^{-1}$ in the LEANDRE II data and the in situ measurements at flight level is apparent. There are several moisture pockets (peak values $> 9 \text{ g kg}^{-1}$) $\sim 1 \text{ km}$ in diameter and separated by 1–2 km east of the dryline. The mechanism that is creating these pools of moisture is not known. The existence of these small pools in the CBL support the claim by Weckwerth et al. (1996) and Weckwerth (2000) that the representativeness of soundings launched from point locations could be questioned.

The discontinuity associated with the dryline has sharpened during the time shown in Fig. 20b. There is now an abrupt shift in wind direction as indicated by the flight-level data and the moisture discontinuity has also increased. The latter observations are primarily a result of the drying of the continental air west of the dryline with mixing ratios retrieved by LEANDRE II now less than 7 g kg^{-1} .

8. Summary and discussion

The evolution and finescale structure of a dryline that initiated a line of thunderstorms were presented. The dryline appeared on radar as a well-defined thin

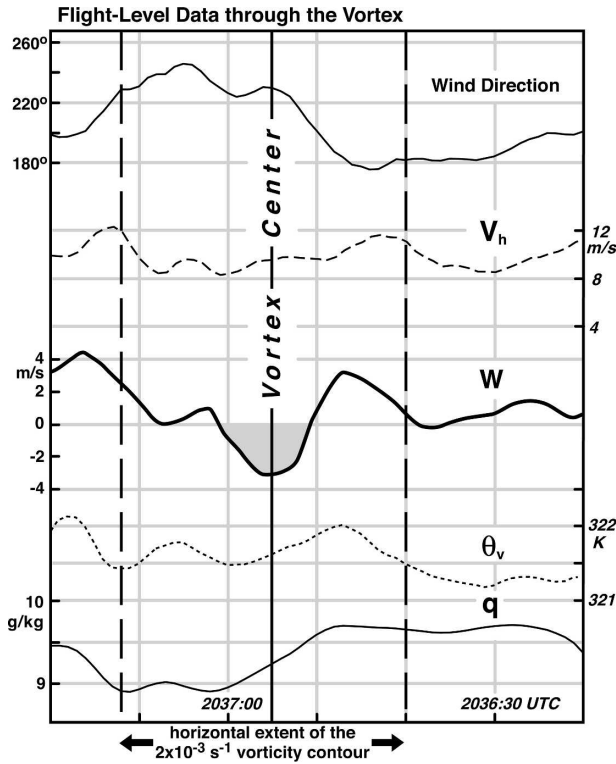


FIG. 16. Flight-level data recorded by the NRL P-3 as it penetrated a circulation along the dryline at ~ 500 m AGL. Wind direction and speed, vertical velocity, virtual potential temperature, and mixing ratio are plotted from 2036:20 to 2037:20 UTC. The approximate vortex center is shown, and the dashed lines represent the horizontal extent of the $2 \times 10^{-3} \text{ s}^{-1}$ vorticity isopleth. Vertical velocities less than 0 m s^{-1} are shaded gray. The location of the circulation is shown in Fig. 8b.

line and was well sampled by an airborne Doppler radar and water vapor DIAL. The flight legs were long (75–80 km), parallel, and close (2–3 km) to the dryline. As a result, both the along-line variability and the mean vertical structure of the dryline could be accurately determined. The latter strongly suggests that the initiation of convection along the dryline at this time appeared to be a result of the diurnally induced easterly flow in the maritime air that typically develops late in the day. This flow increases low-level convergence and allowed rising parcels of air to reach the LFC.

A number of misocyclones were resolved along the dryline and their presence had a major impact on its along-line variability. In general, the misocyclone represents an inflection point in the wind field with enhanced dry westerly and moist easterly flow (relative to the orientation of the dryline) located south and north of the misocyclone, respectively. The updrafts along the dryline were not continuous but occurred in regions that were displaced and generally positioned north of

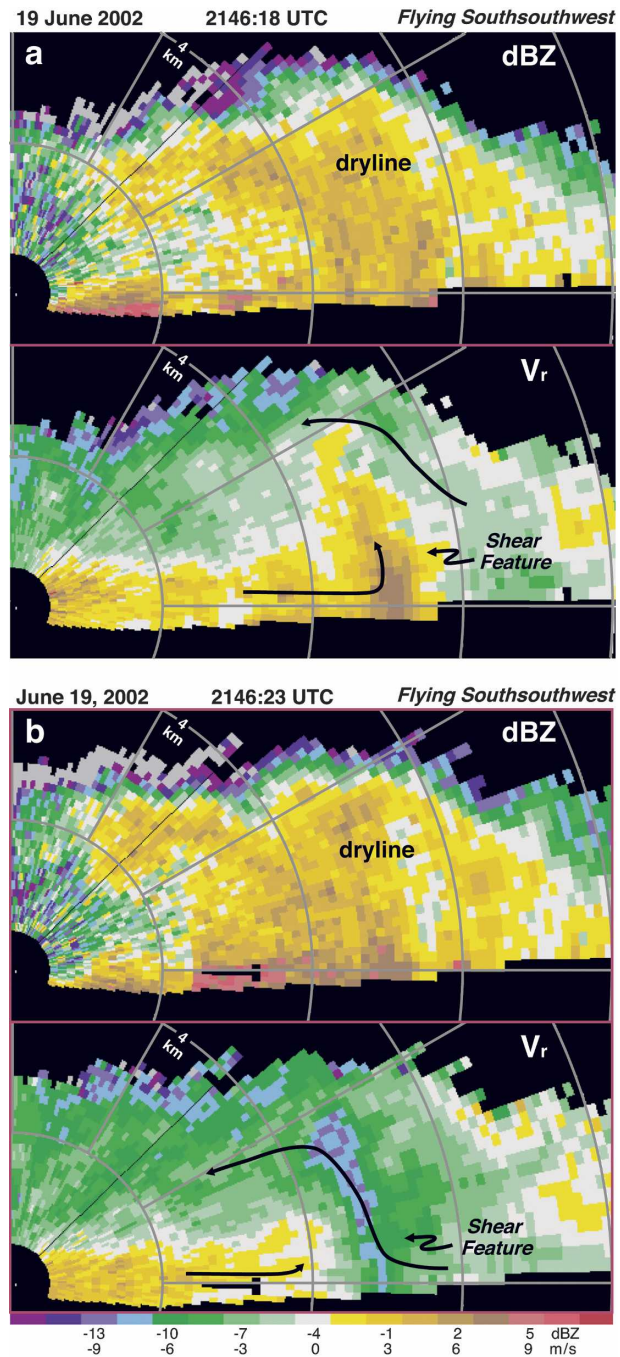


FIG. 17. RHI cross sections of radar reflectivity and single-Doppler velocity through a circulation that developed along the dryline. The images are for consecutive radar scans at (a) 2146:18 and (b) 2146:23 UTC. The RHI scans were taken through the circulation shown in Fig. 11b.

the misocyclone. It was hypothesized that the misocyclones suppressed the updrafts along the dryline by creating a downward-directed perturbation pressure gradient force. In addition, the distortion of the dryline by

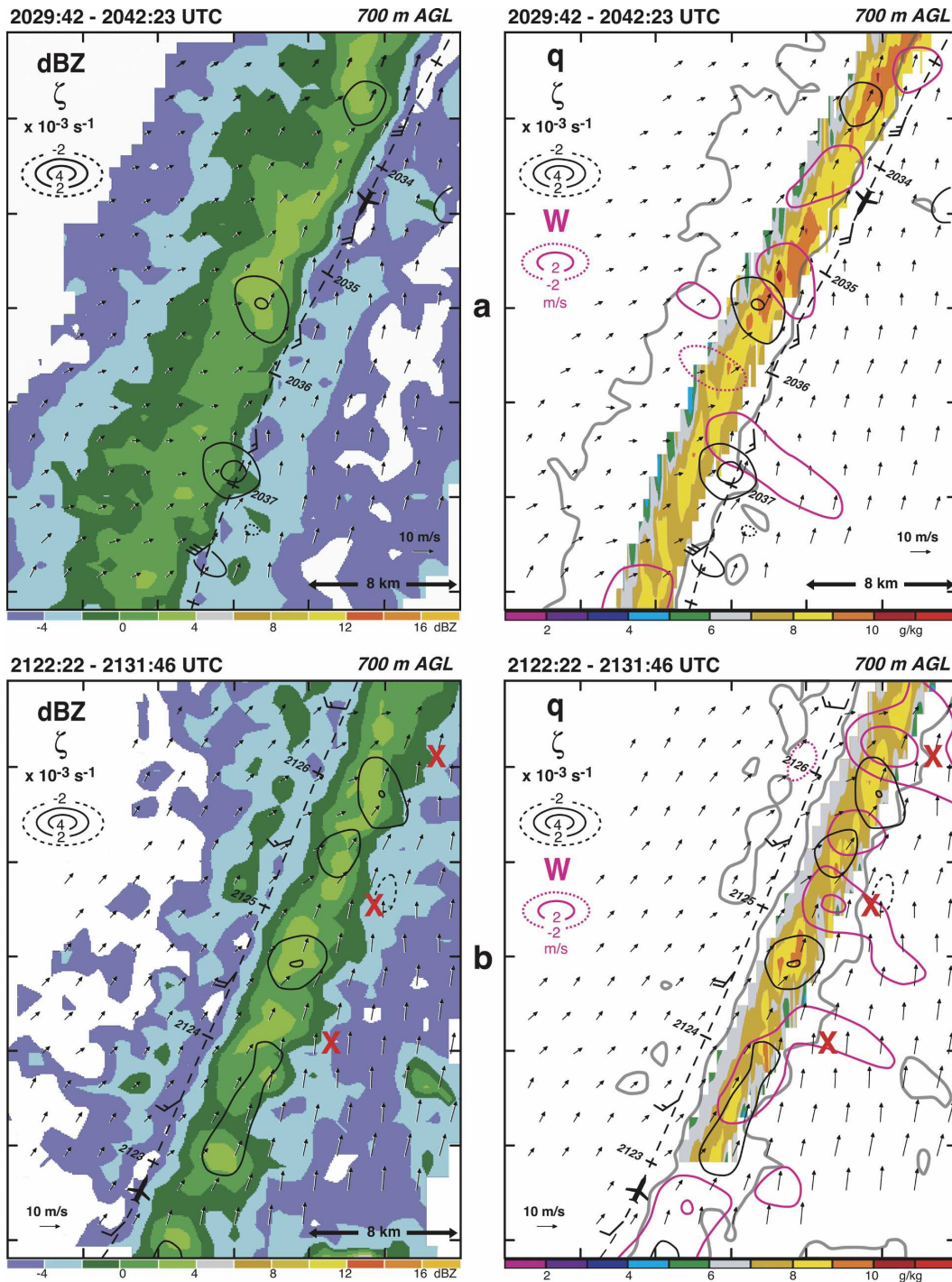


FIG. 18. Dual-Doppler wind syntheses at (a) 2029:42–2042:23 and (b) 2122:22–2131:46 UTC at 700 m AGL: (left) radar reflectivity and vertical vorticity, and (right) vertical vorticity, vertical velocity, and mixing ratios retrieved from LEANDRE II. Red crosses in (b) represent the locations of the peak updrafts into developing storms at 5–8 km AGL. The dashed black line represents the track of the P-3. Flight-level winds are plotted along the track. Wind vectors are plotted with the full barb and half barb representing 5 and 2.5 m s^{-1} , respectively. The -2 dBZ isopleth is plotted as the gray line on the right panels. The locations of the boxes are shown in Figs. 8 and 10.

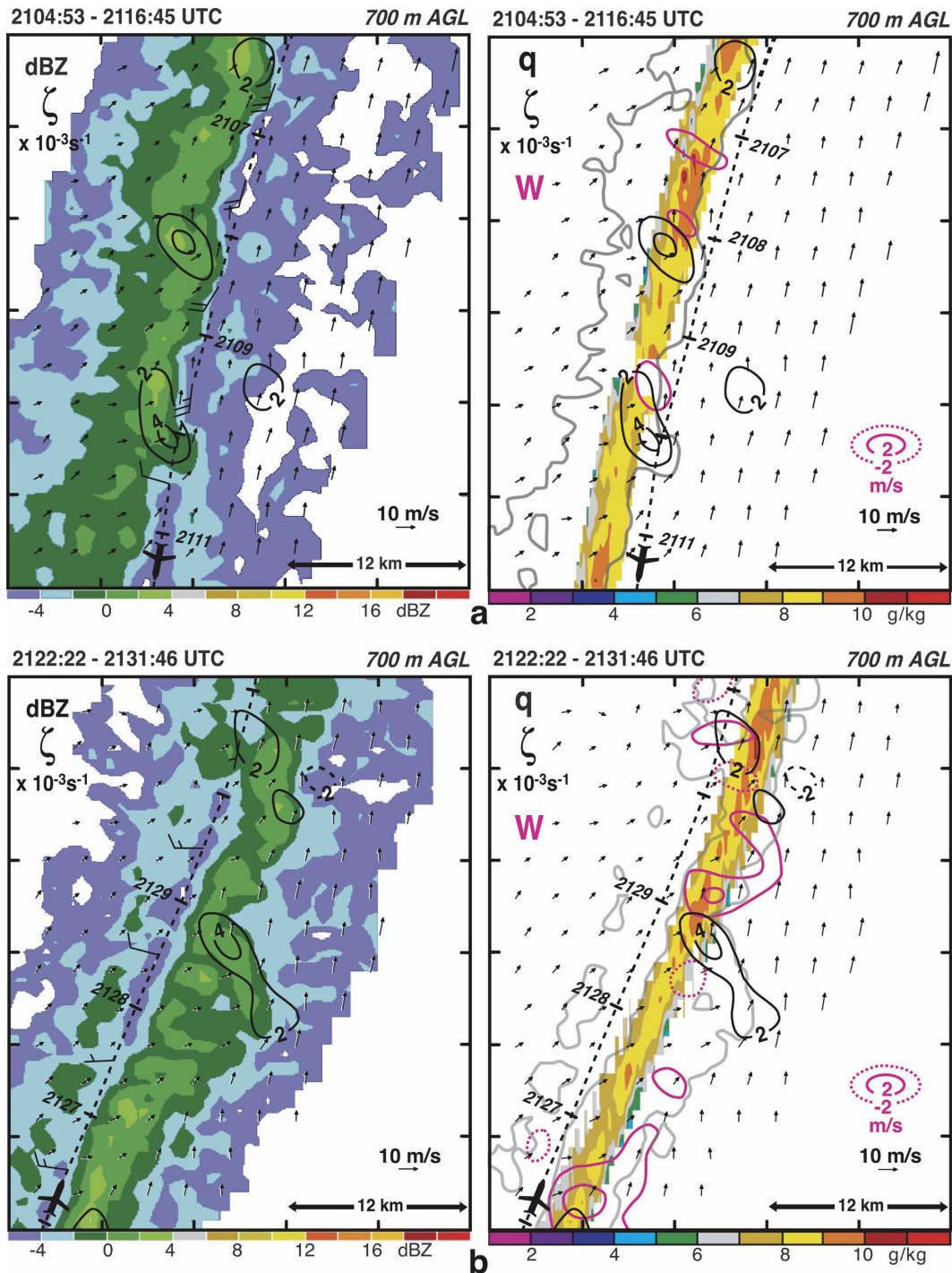


FIG. 19. Dual-Doppler wind syntheses at (a) 2104:53–2116:45 and (b) 2122:22–2131:46 UTC at 700 m AGL: (left) radar reflectivity and vertical vorticity, and (right) vertical vorticity, vertical velocity, and mixing ratios retrieved from LEANDRE II. The dashed black line represents the track of the P-3. Flight-level winds are plotted along the track. Wind vectors are plotted with the full barb and half barb representing 5 and 2.5 m s^{-1} , respectively. The -2 dBZ isopleth is plotted as the gray line on the right panel. The location of the box in (b) is shown in Fig. 10.

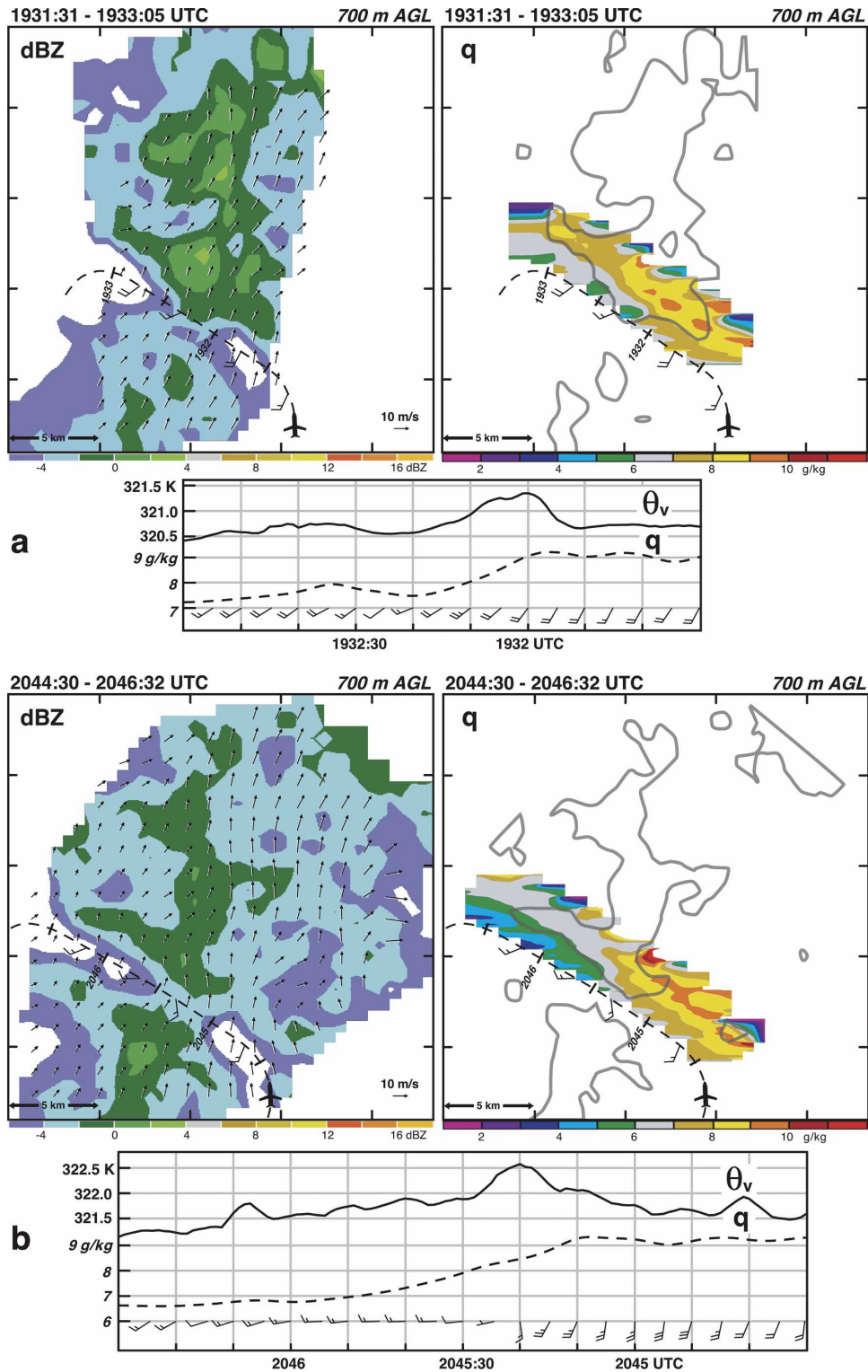


FIG. 20. Dual-Doppler wind syntheses at (a) 1931:31–1933:05 and (b) 2044:30–2046:32 UTC at 700 m AGL: (top left) radar reflectivity, and (top right) mixing ratios retrieved from LEANDRE II. The -2 dBZ isopleth is plotted as the gray line. The dashed black line represents the track of the P-3. Flight-level winds are plotted along the track. Wind vectors are plotted with the full barb and half barb representing 5 and 2.5 m s^{-1} , respectively. Also included are time plots of the flight-level data of virtual potential temperature, mixing ratio, and wind speed and direction during the penetration of the dryline.

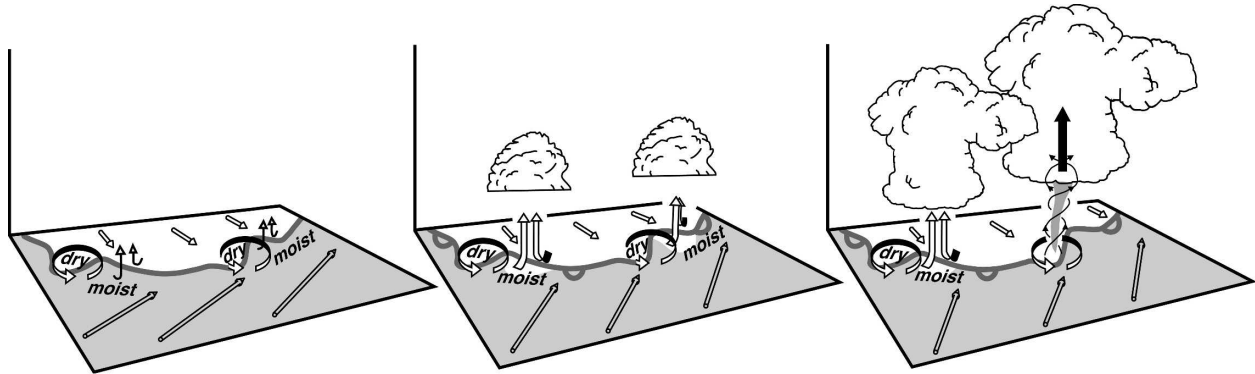


FIG. 21. Schematic model showing the relationship between misocyclones, updrafts, and the horizontal distribution of moisture that lead to the initiation of convection, and nonsupercell tornadogenesis.

the misocyclones resulted in preferred updraft regions. These updrafts were shown to be fortuitously positioned near regions of high mixing ratio where convection first initiated. Accordingly, the misocyclones played a major role in determining where moist parcels of air were being forced up to their LFC. Updrafts tended to be collocated with the misocyclones as the storms grew. This superposition occurred at a time when dust devils and tornado-like circulations were observed. The generating mechanism of these intense circulations was believed to be the same as for nonsupercell tornadoes. These observations are summarized in the schematic model presented in Fig. 21. Part II of this paper will present even higher resolution data of the dryline on 19 June using the ground-based mobile facilities. The detailed structure of the misocyclones will be presented.

Acknowledgments. The authors thank Jim Wilson (NCAR) and Nolan Atkins (Lyndon State College) for their thoughtful reviews. Their suggestions greatly improved an earlier version of this manuscript. We also wish to thank the U.S. Navy pilots and crew of the NRL P-3, as well as the engineers and technicians from ATD/NCAR, that operated the equipment on board the aircraft. The first author also would like to thank Wen-Chau Lee (NCAR) and Michael Bell (NCAR) for endless support with the ELDORA dataset. Research results presented in this paper were supported by the National Science Foundation under Grant ATM-021048 (through RMW) and Grants ATM-9901688 and ATM-0432951 (through DEK).

APPENDIX

Radar Methodology

The radar data were edited and the aircraft motion was removed from the velocity fields using the SOLO II

software package (Oye et al. 1995). The data were then corrected for navigational errors using a technique developed by Testud et al. (1995). The along-track and sweep-angle resolution for ELDORA during IHOP was ~ 550 m and 1.5° , respectively, based on the information presented in Table 1. This led to an effective sampling in the vertical of ~ 250 m at a distance of 10 km from the radar. The data were subsequently interpolated onto a grid with a horizontal and vertical grid spacing of 600 and 300 m, respectively. A Cressman filter (Cressman 1959) was applied during the interpolation process with a radius of influence of 600 m in the horizontal and 450 m in the vertical. The lowest level was chosen to be 400 m AGL. Since the dryline was quasi-stationary during the observational period, the data were not time-space adjusted.

The synthesis of the radar data was performed using Custom Editing and Display of Reduced Information in Cartesian Space (CEDRIC; Mohr et al. 1986). A two-step Leise filter (Leise 1982) was applied to the Doppler wind field. This effectively removes wavelengths of less than 2.4 km. The hydrometeor fall speeds were estimated from the reflectivity-terminal fall speed relationship established by Joss and Waldvogel (1970) with a correction for the effects of air density (Foote and du Toit 1969). The vertical velocities were derived from an upward integration of the horizontal convergence field of the anelastic continuity equation. The errors associated with the vertical velocities are estimated to be less than $1\text{--}2\text{ m s}^{-1}$ (Wilson et al. 1994). These uncertainties will be reduced in the mean vertical cross sections that were created. All wind fields shown in the paper are ground relative. The misocyclones documented in this paper are close to the resolvable wavelength of the synthesized wind field. Accordingly, the peak vertical vorticities and velocities are underestimated.

REFERENCES

- Atkins, N. T., R. M. Wakimoto, and T. M. Weckwerth, 1995: Observations of the sea-breeze front during CaPE. Part II: Dual-Doppler and aircraft analysis. *Mon. Wea. Rev.*, **123**, 944–969.
- , —, and C. L. Ziegler, 1998: Observations of the finescale structure of a dryline during VORTEX 95. *Mon. Wea. Rev.*, **126**, 525–550.
- Atlas, D., 1959: Meteorological “angel” echoes. *J. Meteor.*, **16**, 6–11.
- Barnes, S. L., 1973: Mesoscale objective map analysis using weighted time-series observations. NOAA Tech. Memo. ERL NSSL-62, 60 pp. [Available from the National Severe Storms Laboratory, 1313 Halley Circle, Norman, OK 73069.]
- Bluestein, H. B., E. W. McCaul, G. P. Byrd, and G. R. Woodall, 1988: Mobile sounding observation of a tornadic storm near the dryline: The Canadian, Texas storm of 7 May 1986. *Mon. Wea. Rev.*, **116**, 1790–1804.
- Brady, R. H., and E. J. Szoke, 1989: A case study of non-mesocyclone tornado development in northeast Colorado: Similarities to waterspout formation. *Mon. Wea. Rev.*, **117**, 843–856.
- Bruneau, D., P. Quaglia, C. Flamant, M. Meissonnier, and J. Pelon, 2001: Airborne lidar LEANDRE II for water-vapor profiling in the troposphere. *Appl. Opt.*, **40**, 3450–3475.
- Carbone, R. E., 1982: A severe frontal rainband. Part I: Storm-wide hydrodynamic structure. *J. Atmos. Sci.*, **39**, 258–279.
- Christian, T. W., and R. M. Wakimoto, 1989: The relationship between radar reflectivity and clouds associated with horizontal convective rolls. *Mon. Wea. Rev.*, **117**, 1530–1544.
- Crawford, T. M., and H. B. Bluestein, 1997: Characteristics of dryline passage during COPS-91. *Mon. Wea. Rev.*, **125**, 463–477.
- Cressman, G. P., 1959: An operational objective analysis scheme. *Mon. Wea. Rev.*, **87**, 367–384.
- Crook, N. A., 1996: Sensitivity of moist convection forced by boundary layer processes to low-level thermodynamic fields. *Mon. Wea. Rev.*, **124**, 1767–1785.
- , and J. B. Klemp, 2000: Lifting by convergence lines. *J. Atmos. Sci.*, **57**, 873–890.
- Fankhauser, J. C., N. A. Crook, J. Tuttle, L. J. Miller, and C. G. Wade, 1995: Initiation of deep convection along boundary layer convergence lines in a semitropical environment. *Mon. Wea. Rev.*, **123**, 291–313.
- Foote, G. B., and R. S. du Toit, 1969: Terminal velocity of raindrops aloft. *J. Appl. Meteor.*, **8**, 249–253.
- Fujita, T. T., 1981: Tornadoes and downbursts in the context of generalized planetary scales. *J. Atmos. Sci.*, **38**, 1511–1534.
- Hane, C. E., C. L. Ziegler, and H. B. Bluestein, 1993: Investigation of the dryline and convective storms initiated along the dryline: Field experiments during COPS-91. *Bull. Amer. Meteor. Soc.*, **74**, 2133–2145.
- , H. B. Bluestein, T. M. Crawford, M. E. Baldwin, and R. M. Rabin, 1997: Severe thunderstorm development in relation to along-dryline variability: A case study. *Mon. Wea. Rev.*, **125**, 231–251.
- , R. M. Rabin, T. M. Crawford, H. B. Bluestein, and M. E. Baldwin, 2002: A case study of severe storm development along a dryline within a synoptically active environment. Part II: Multiple boundaries and convective initiation. *Mon. Wea. Rev.*, **130**, 900–920.
- Hildebrand, P. H., C. A. Walther, C. L. Frush, J. Testud, and F. Baudin, 1994: The ELDORA/ASTRAIA airborne Doppler weather radar: Goals, design and first field tests. *Proc. IEEE*, **82**, 1873–1890.
- , and Coauthors, 1996: The ELDORA/ASTRAIA airborne Doppler weather radar: High-resolution observations from TOGA COARE. *Bull. Amer. Meteor. Soc.*, **77**, 213–232.
- Hobbs, P. V., and P. O. G. Persson, 1982: The mesoscale and microscale structure and organization of clouds and precipitation in midlatitude cyclones. Part V: The substructure of narrow cold-frontal rainbands. *J. Atmos. Sci.*, **39**, 280–295.
- Jones, P. A., and P. R. Bannon, 2002: A mixed-layer model of the diurnal dryline. *J. Atmos. Sci.*, **59**, 2582–2593.
- Jorgensen, D. P., T. Matejka, and J. D. DuGranrut, 1996: Multi-beam techniques for deriving wind fields from airborne Doppler radars. *J. Meteor. Atmos. Phys.*, **59**, 83–104.
- Joss, J., and D. Waldvogel, 1970: Raindrop size distribution and Doppler velocities. Preprints, *14th Conf. on Radar Meteorology*, Tucson, AZ, Amer. Meteor. Soc., 153–156.
- Kingsmill, D. E., 1995: Convection initiation associated with a sea-breeze front, a gust front, and their collision. *Mon. Wea. Rev.*, **123**, 2913–2933.
- Klemp, J. B., and R. Rotunno, 1983: A study of the tornadic region within a supercell thunderstorm. *J. Atmos. Sci.*, **40**, 359–377.
- Knight, C. A., and L. J. Miller, 1993: First echoes from cumulus clouds. *Bull. Amer. Meteor. Soc.*, **74**, 179–188.
- Koch, S. E., 1982: The role of apparent gravity waves as a triggering mechanism for severe thunderstorm along a dryline. Preprints, *12th Conf. on Severe Local Storms*, San Antonio, TX, Amer. Meteor. Soc., 573–576.
- , and J. McCarthy, 1982: The evolution of an Oklahoma dryline. Part II: Boundary-layer forcing of mesoconvective systems. *J. Atmos. Sci.*, **39**, 237–257.
- Lee, B. D., and R. B. Wilhelmson, 1997: The numerical simulation of non-supercell tornadogenesis. Part I: Initiation and evolution of pretornadic mesocyclone circulations along a dry outflow boundary. *J. Atmos. Sci.*, **54**, 32–60.
- , R. D. Farley, and M. R. Hjelmfelt, 1991: A numerical case study of convection initiation along colliding convergence boundaries in northeast Colorado. *J. Atmos. Sci.*, **48**, 2350–2366.
- Leise, J. A., 1982: A multidimensional scale-telescoped filter and data extension package. NOAA Tech. Memo. ERL-82, 11 pp. [Available from NOAA ERL, 325 Broadway, Boulder, CO 80303.]
- Miles, J. W., and L. N. Howard, 1964: Note on heterogeneous shear flow. *J. Fluid Mech.*, **20**, 331–336.
- Miller, J. A., T. A. Kovacs, and P. R. Bannon, 2001: A shallow-water model of the diurnal dryline. *J. Atmos. Sci.*, **58**, 3508–3524.
- Mohr, C. G., L. J. Miller, R. L. Vaughn, and H. W. Frank, 1986: The merger of mesoscale datasets into a common Cartesian format for efficient and systematic analysis. *J. Atmos. Oceanic Technol.*, **3**, 146–161.
- Mueller, C. K., and R. Carbone, 1987: Dynamics of a thunderstorm outflow. *J. Atmos. Sci.*, **44**, 1879–1898.
- Olsen, D. A., N. W. Junker, and B. Korty, 1995: Evaluation of 33 years of quantitative precipitation forecasting at the NMC. *Wea. Forecasting*, **10**, 498–511.
- Oye, R., C. Mueller, and S. Smith, 1995: Software for radar translation, visualization, editing, and interpolation. Preprints, *27th Conf. on Radar Meteorology*, Vail, CO, Amer. Meteor. Soc., 359–361.
- Purdum, J. F., 1976: Some uses of high-resolution GOES imagery

- in the mesoscale forecasting of convection and its behavior. *Mon. Wea. Rev.*, **104**, 1474–1483.
- , 1982: Subjective interpretation of geostationary satellite data for nowcasting. *Nowcasting*, K. Browning, Ed., Academic Press, 149–166.
- Rhea, J. O., 1966: A study of thunderstorm formation along dry lines. *J. Appl. Meteor.*, **5**, 58–63.
- Rotunno, R., J. B. Klemp, and M. L. Weisman, 1988: A theory for strong, long-lived squall lines. *J. Atmos. Sci.*, **45**, 463–485.
- Schaefer, J. T., 1974: The life cycle of the dryline. *J. Appl. Meteor.*, **13**, 444–449.
- , 1986: The dryline. *Mesoscale Meteorology and Forecasting*, P. S. Ray, Ed., Amer. Meteor. Soc., 549–572.
- Stensrud, D. J., and R. A. Maddox, 1988: Opposing mesoscale circulations: A case study. *Wea. Forecasting*, **3**, 189–204.
- Testud, J., P. H. Hildebrand, and W.-C. Lee, 1995: A procedure to correct airborne Doppler radar data for navigation errors using the echo returned from the earth's surface. *J. Atmos. Oceanic Technol.*, **12**, 800–820.
- Wakimoto, R. M., and J. W. Wilson, 1989: Non-supercell tornadoes. *Mon. Wea. Rev.*, **117**, 1113–1140.
- , and B. L. Bosart, 2000: Airborne radar observations of a cold front during FASTEX. *Mon. Wea. Rev.*, **128**, 2447–2470.
- , W.-C. Lee, H. B. Bluestein, C.-H. Liu, and P. H. Hildebrand, 1996: ELDORA observations during VORTEX 95. *Bull. Amer. Meteor. Soc.*, **77**, 1465–1481.
- , H. V. Murphey, R. G. Fovell, and W.-C. Lee, 2004: Mantle echoes associated with deep convection: Observations and numerical simulations. *Mon. Wea. Rev.*, **132**, 1701–1720.
- Weckwerth, T. M., 2000: The effect of small-scale moisture variability on thunderstorm initiation. *Mon. Wea. Rev.*, **128**, 4017–4030.
- , and R. M. Wakimoto, 1992: The initiation and organization of convective cells atop a cold-air outflow boundary. *Mon. Wea. Rev.*, **120**, 2169–2187.
- , J. W. Wilson, and R. M. Wakimoto, 1996: Thermodynamic variability within the convective boundary layer due to horizontal convective rolls. *Mon. Wea. Rev.*, **124**, 769–784.
- , and Coauthors, 2004: An overview of the International H₂O Project (IHOP_2002) and some preliminary highlights. *Bull. Amer. Meteor. Soc.*, **85**, 253–277.
- Weisman, M. L., and J. B. Klemp, 1982: The dependence of numerically simulated convective storms on vertical wind shear and buoyancy. *Mon. Wea. Rev.*, **110**, 504–520.
- Wilson, J. W., and W. E. Schreiber, 1986: Initiation of convective storms at radar observed boundary-layer convergence lines. *Mon. Wea. Rev.*, **114**, 2516–2536.
- , and C. K. Mueller, 1993: Nowcasts of thunderstorm initiation and evolution. *Wea. Forecasting*, **8**, 113–131.
- , and D. L. Meigenhardt, 1997: Thunderstorm initiation, organization, and lifetime associated with Florida boundary layer convergence lines. *Mon. Wea. Rev.*, **125**, 1507–1525.
- , G. B. Foote, N. A. Crook, J. C. Fankhauser, C. G. Wade, J. D. Tuttle, and C. K. Mueller, 1992: The role of boundary-layer convergence zones and horizontal rolls in the initiation of thunderstorms: A case study. *Mon. Wea. Rev.*, **120**, 1785–1815.
- , T. M. Weckwerth, J. Vivekanandan, R. M. Wakimoto, and R. W. Russell, 1994: Boundary layer clear-air echoes: Origin of echoes and accuracy of derived winds. *J. Atmos. Oceanic Technol.*, **11**, 1184–1206.
- , N. A. Crook, C. K. Mueller, J. Sun, and M. Dixon, 1998: Nowcasting thunderstorms: A status report. *Bull. Amer. Meteor. Soc.*, **79**, 2079–2099.
- Ziegler, C. L., and C. E. Hane, 1993: An observational study of the dryline. *Mon. Wea. Rev.*, **121**, 1134–1151.
- , and E. N. Rasmussen, 1998: The initiation of moist convection at the dryline: Forecasting issues from a case study perspective. *Wea. Forecasting*, **13**, 1106–1131.
- , W. J. Martin, R. A. Pielke, and R. L. Walko, 1995: A modeling study of the dryline. *J. Atmos. Sci.*, **52**, 263–284.
- , T. J. Lee, and R. A. Pielke, 1997: Convective initiation at the dryline: A modeling study. *Mon. Wea. Rev.*, **125**, 1001–1026.